Separation and Purification Technology 424 (2027) 140736

Contents lists available at ScienceDirect

Separation and Purification Technology

journal homepage: www.elsevier.com/locate/seppur

Selective silicon removal from Al—Si scraps by Mg-assisted electromagnetic fractional crystallization

Bo Yang, Semiramis Friedrich *, Bernd Friedrich

IME Process Metallurgy and Metal Recycling, RWTH Aachen University, 52056 Aachen, Germany

ARTICLE INFO

Keywords:
Al—Si scraps
Upcycling
Si removal
Mg addition
Alternating electromagnetic field
Fractional crystallization

ABSTRACT

In the context of the transition toward vehicle electrification and lightweighting, end-of-life Al—Si casting scrap is increasingly at risk of becoming "dead metal" because its high Si content prevents direct reuse in high-value aluminum products. In this study, an integrated Mg-assisted electromagnetic fractional crystallization route was developed to upcycle Al—Si scrap. Thermochemical calculations demonstrated that Mg addition modifies the solidification path by converting eutectic Si into separable primary Mg_2Si. Experiments using an Al-6.45%Si-28.54%Mg alloy showed that the Si content in the purified region decreased to 0.406 wt% under natural cooling, achieving a Si removal efficiency of 93.71%, which is close to the thermochemical prediction. However, the purified region area fraction was only 17.8%. The application of the electromagnetic field following the initial Mg_2Si formation exhibited a negligible effect on the purified-region yield. In contrast, the application of a continuous alternating electromagnetic field during primary Mg_2Si precipitation resulted in a significant enhancement of phase separation. As the coil current increased from 330 to 430 and 530 A, the central purified-region area fraction increased from 71.15% to 78.30% and 79.50%, while maintaining a high Si removal efficiency of 93.36–93.76%. The separation mechanism is attributed to the Mg-induced phase transformation, Lorentz force-driven convection, electromagnetic-assisted Mg_2Si migration, and preferential growth near the colder crucible wall. The resulting low-Si Al—Mg alloy could subsequently be treated by vacuum distillation to remove Mg, while the recovered Mg could be recycled in the upstream crystallization process. The present study proposes a promising and potentially scalable circular-economy route for upcycling Al—Si casting scrap into high-value aluminum alloy products.

1. Introduction

Hypoeutectic Al—Si alloys are indispensable in transportation and aerospace applications due to their excellent castability, fatigue resistance, and high specific strength [1–3]. While Si improves the fluidity and castability of Al alloys during casting, the associated formation of eutectic Si phases inevitably constrains their mechanical properties [4,5]. Specifically, the low solubility (0.05 at.%, 300 °C [6,7]) of silicon in aluminum leads to the formation of coarse and brittle plate-like Si phases after solidification, which significantly reduces the ductility and fracture resistance [8–10].

Aluminum recycling offers substantial economic and environmental benefits. As one of the most recyclable structural materials, Al recycling consumes only about 5% of the energy required for primary aluminum production and reduces greenhouse gas emissions by approximately 95% [11–13]. Despite these advantages, conventional remelting-based recycling is intrinsically limited in its ability to remove most impurities due to the thermochemical constraints [14]. As recycling cycles proceed, alloying elements accumulate in secondary aluminum streams, resulting in progressive material down-cycling [15,16]. In the automotive sector, the ongoing shift toward electrification and lightweighting is driving material demand from impurity-tolerant cast alloys toward wrought alloys with tighter compositional limits [17–19]. Consequently, future recycling loops will have a lower tolerance for impurity elements. The demand for wrought aluminum alloys in automotive applications is projected to increase by approximately 4–20 times by 2050, whereas the demand for cast aluminum alloys in the no-lightweight-transition scenario is expected to decline to only 0.7–0.9 times the current level [20]. Since the automotive market has been dominated by internal combustion engine vehicles (ICEVs) over past decades, large quantities of end-of-life Al—Si cast scrap derived from engine blocks and transmission housings will emerge as these vehicles retire, leading to a

* Corresponding author.
E-mail address: SFriedrich@ime-aachen.de (S. Friedrich).

https://doi.org/10.1016/j.seppur.2026.140736
Received 21 August 2026; Received in revised form 13 October 2026; Accepted 27 October 2026
Available online 30 October 2026
1383-5866/© 2026 The Authors. Published by Elsevier B.V. This is an open access article under the CC BY license (http://creativecommons.org/licenses/by/4.0/).
Open access funding enabled and organized by Projekt DEAL.

substantial future surplus of such alloys [20,21]. By 2050, the surplus of Al cast scrap is projected to range from 3.3 million to 18.3 million tons [22]. Due to their high Si content, these alloys cannot be directly reused for wrought Al alloys required in electric vehicles, which will become "dead metal" [23–25]. Therefore, developing efficient upcycling strategies to remove silicon from Al—Si scrap is essential for enabling closed-loop recycling of aluminum alloys.

The removal of Si from Al—Si alloys is intrinsically challenging because of the solidification characteristics of these systems. To be specific, in hypoeutectic and eutectic Al—Si alloys, silicon typically forms eutectic structures that grow cooperatively with the α-Al matrix during solidification [26]. The resulting plate-like or fibrous eutectic Si network is strongly interconnected with the α-Al dendrites, making phase separation extremely difficult under conventional solidification conditions [27] Various approaches have been explored to separate silicon from aluminum melts, including electrochemical routes [28–30], semi-solid centrifugal separation [31,32], electromagnetic (EM) force-assisted directional solidification [27,33]. However, each approach presents inherent limitations. Despite its strong purification capability, electrochemical routes still face substantial challenges associated with molten-salt handling, corrosion, cell complexity, and environmental burden [34]. Moreover, although solid-state electrolysis can reduce the energy demand to less than half that of primary aluminum production, its specific energy consumption (65.4 $MJkg^{-1}$ Al) remains about an order of magnitude higher than that of conventional remelting-based recycling (~5 $MJkg^{-1}$ Al) [29]. Semi-solid centrifugal separation operates within a narrow processing window and often suffers from a trade-off between impurity removal efficiency and metal yield, while also requiring high-speed rotational equipment that complicates industrial scaling. Electromagnetic force-assisted directional solidification can achieve Si segregation, but excessive electromagnetic forces may destabilize the solidification front, leading to ingot fragmentation and separation failure. Furthermore, conventional induction-coil-generated electromagnetic fields alone often provide insufficient driving force for effective Si separation [35]. The limitations of these methods indicate that simultaneously achieving high Si removal efficiency, high metal yield, and low energy consumption remains a major challenge for Al—Si scrap upcycling. Therefore, developing simpler and more energy-efficient metallurgical strategies is essential for the scalable upcycling of Al—Si scrap.

A suspension-based fractional crystallization strategy assisted by magnesium addition was proposed for silicon removal from Al—Si melts in our previous work [36]. When sufficient Mg was introduced, silicon preferentially precipitated as primary Mg_2Si intermetallic compounds, which could subsequently separate from the melt due to density differences. This approach demonstrated the feasibility of converting silicon into an extractable carrier phase and separating it from the aluminum melt. However, the separation of primary Mg_2Si in this process mainly relies on buoyancy-driven flotation, which may limit the efficiency of particle enrichment and the yield of purified Al. Magnetic fields have been widely applied in metallurgical processes for microstructure control and melt purification [37–39]. In electrically conductive melts, alternating magnetic fields generate Lorentz and thermoelectric magnetic forces through electromagnetic induction, which can modify melt convection, enhance solute transport, and drive the migration and redistribution of intermetallic particles via electromagnetic stirring and magnetohydrodynamic flow [40–42]. These effects provide a promising opportunity to actively regulate the migration and aggregation of Mg_2Si particles during solidification.

In this work, a novel upcycling strategy was developed for Si removal from Al—Si scrap by Mg-assisted electromagnetic (EM) fractional crystallization. The study systematically investigated the effects of key process parameters on phase separation and metal recovery. It investigates whether Mg addition enable to transform dissolved Si into separable primary Mg_2Si phase, and combines this effect with the application of a continuous alternating magnetic field to induce electromagnetic forces that promote the enrichment and separation of primary Mg_2Si. The mechanism of primary Mg_2Si formation and electromagnetic-assisted enrichment was elucidated. Subsequently, vacuum treatment can be applied to recover excess Mg from the low-Si Al—Mg product after Si removal, ultimately enabling the upcycling of Al—Si scrap into high-value aluminum alloy products.

2. Experimental

2.1. Material preparation

In order to investigate the Si removal mechanism more clearly, a binary Al-9%Si alloy was chosen as a representative model material for Al—Si casting scrap, because Al-9%Si is representative of hypoeutectic automotive casting alloys such as engine blocks and transmission housings. The base Al-9%Si alloy was prepared from pure Al (99.9%) and Al-20%Si master alloy. Unless otherwise specified, all compositions reported in this work are given in weight percent (wt%). The as-prepared Al-9%Si alloy was then alloyed with pure Mg (99.95%) at a mass ratio of 1:0.4 to obtain the target Al-6.4%Si-28.6%Mg alloy. The measured chemical composition of the experimentally prepared Al-Si-Mg alloy is summarized in Table 1.

2.2. Experimental equipment and process

To prepare the Al-9%Si alloy, a certain amount of pure Al and Al-20%Si master alloy were charged into an A10 clay-graphite crucible and melted in an induction furnace to 750 °C. The main constituents of the clay-graphite crucible are 40–47 wt% C, 10–18 wt% SiC, 10–18 wt% Al_2O_3, and 20–30 wt% SiO_2, with an open porosity of 29–30 vol%. A continuous flow of high-purity Ar was applied above the melt surface through a gas delivery tube to provide a protective atmosphere and prevent oxidation of the melt. The melt was held for 20 min to ensure complete melting and chemical homogenization. The crucible surface in contact with the melt was coated with boron nitride (BN) to reduce direct melt-crucible interaction and suppress possible contamination during high-temperature processing. The melt temperature was continuously monitored using a K-type thermocouple protected by a ceramic sheath and recorded by a digital data acquisition system. The thermocouple was positioned at the center of the melt. After the Al-9%Si melt had been fully homogenized, and before the stepwise addition of magnesium, a salt flux was added onto the melt surface to establish a protective layer. The commercial Mg-salt flux (Flux 5), composed of approximately 46 wt% $MgCl_2$, 23 wt% KCl, 26 wt% NaCl, and 5 wt% CaF_2, served primarily to suppress Mg oxidation and volatilization. B, Na, Ca and K remained below 10 ppm before and after melting, indicating negligible contamination from the BN-coated crucible and salt flux by these elements. During Mg addition, the melt was protected by the combined action of the salt layer and a high-purity Argon atmosphere. After Mg addition, the melt was reheated to 750 °C and held for another 20 min to promote complete dissolution of Mg and compositional homogenization, thereby producing the target Al-Si-Mg alloy. The overall experimental route is schematically illustrated in Fig. 1.

The Mg-assisted electromagnetic fractional crystallization experiments were subsequently conducted in the same induction furnace. Since the magnetic flux density within the molten alloy could not be measured directly, the alternating current in the induction coil was

Table 1
The chemical composition of the experimentally prepared Al-Si-Mg alloy.

Alloy	Element, wt%			
	Si	Mg	Cu, Zn, Cr, Ni, B, etc	Al
Al-Si alloy	9.07	<0.001	<0.02	Bal.
Al-Si-Mg alloy	6.45	28.54	<0.02	Bal.

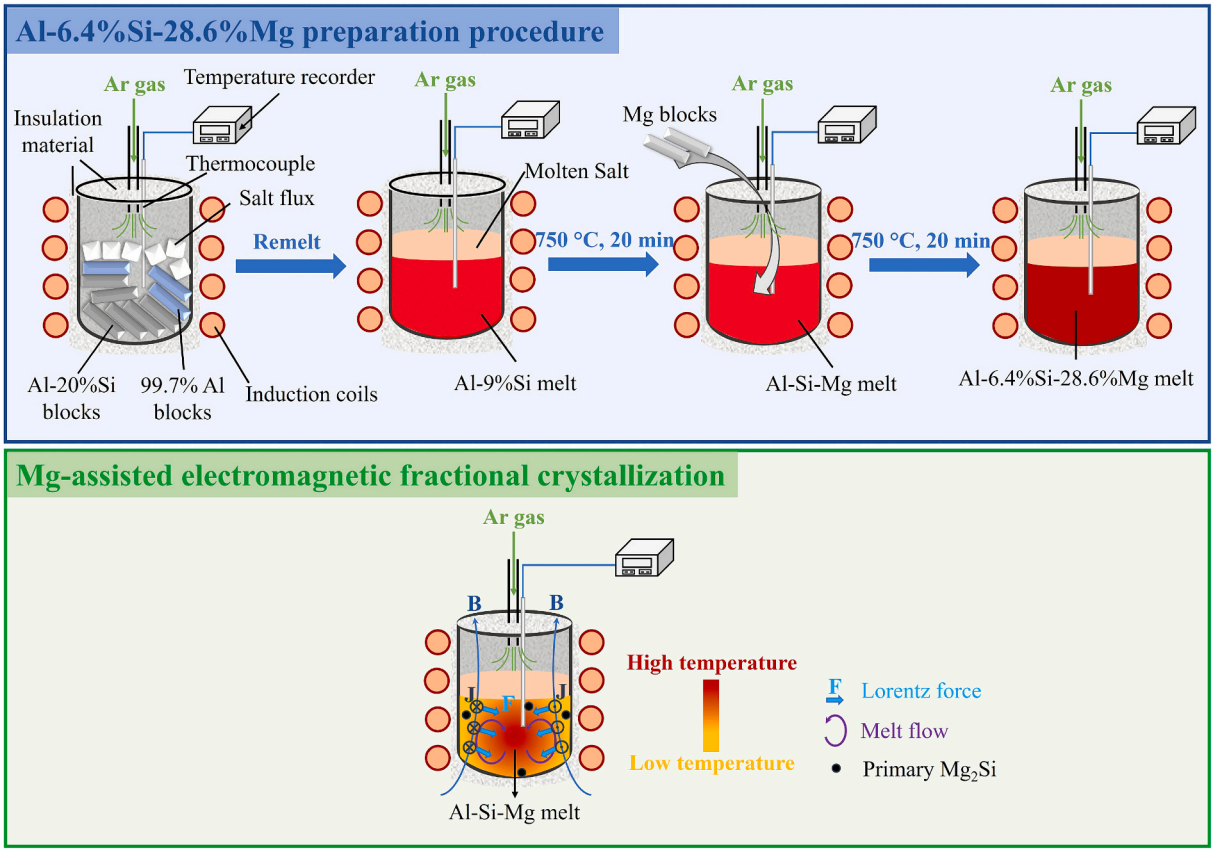


Fig. 1. Schematic diagram of the experimental route: alloy preparation and Mg-assisted electromagnetic fractional crystallization.

measured using a flexible AC current probe (i3000s Flex-24, Fluke). Under the fixed coil geometry and operating frequency, the measured coil current served as an indirect indicator of the applied electromagnetic field intensity. The solidification behavior of the Al-6.4%Si-28.6% Mg alloy was calculated using the Equilib module of FactSage 8.3 with the FTlite database under Scheil-Gulliver conditions. Primary Mg_2Si was predicted to precipitate between 731.8 °C to 535.9 °C, which guided the selection of the experimental temperature window. To elucidate the effect of the alternating magnetic on phase separation, three processing modes were investigated. In the without electromagnetic model, the induction power was switched off directly after the preparation of Al-Si-Mg melt, which was then cooled down naturally. The resulting sample was denoted as #Without EM. In the delayed EM mode, the melt was first cooled naturally from 750 °C to 535 °C, allowing primary Mg_2Si to form before EM treatment. Upon reaching 535 °C, the induction power was turned on and the EM field was applied for a duration. The two samples in this mode were designated as #530 A-90S and #430 A-10 min, representing electromagnetic-field treatment applied after the melt had cooled to 535 °C, at a coil current of 530 A for 90 s and 430 A for 10 min, respectively. In the continuous EM mode, a prescribed coil current of 330, 430, or 530 A was established immediately after melt preparation and maintained while the melt cooled from 750 to 535 °C. Under this condition, the primary Mg_2Si precipitates under the continuous EM. The samples in this mode were labeled as #330 A, #430 A and #530 A, respectively. The corresponding experimental conditions are provided in Table 2. The average cooling rate over 750–535 °C was determined from the recorded temperature-time data. For the without-EM and delayed-EM modes, in which no EM field was applied during this cooling interval, the average cooling rate was approximately 6–7 °C/min. Under continuous EM application, the average cooling rates were 3.79, 2.17, and 1.95 °C/min at coil currents of 330, 430, and 530 A, respectively. Because the coil current simultaneously determined the electromagnetic conditions and induction heat input, these cooling rates represent the actual thermal response of the system rather than independently prescribed parameters. In all cases, the melt was cooled to slightly below the calculated terminal precipitation temperature to ensure complete precipitation of primary Mg_2Si. After completion of the electromagnetic treatment, the crucible containing the melt was removed from the induction coil and rapidly cooled in air to room temperature. After complete cooling, the samples were collected for subsequent characterization.

Table 2
Experimental parameters of Mg-assisted electromagnetic fractional crystallization.

Treatment model	Sample number	EM application temperature stage	Coil current / A	EM duration
Without EM	#without EM	/	/	/
Delayed EM	#530 A-90s	535 °C	530	90 s
	#430 A-10 min	535 °C	430	10 min
Continuous EM	#330 A	750 °C → 535 °C	330	Continuous
	#430 A	750 °C → 535 °C	430	Continuous
	#530 A	750 °C → 535 °C	530	Continuous

2.3. Characterization

The chemical compositions of the raw materials, intermediate products, and final products were analyzed by inductively coupled plasma optical emission spectroscopy (ICP-OES, Agilent 5900 SVDV) and Spectro spark spectometer MAXx (SPECTRO Analytical Instruments). The measured results were used to quantify Si and Mg

redistribution and to calculate the corresponding removal efficiencies.

Based on the measured Si and Mg contents, the removal efficiency of each element (η_i) was calculated with the following equation:

$$\eta_i = \frac{C_{0,i} - C_{p,i}}{C_{0,i}} \times 100\% \quad (1)$$

where $C_{0,i}$ and $C_{p,i}$ are the Si or Mg content (wt%) in the initial Al-Si-Mg samples and the purified region of the sample after Mg-assisted electromagnetic fractional crystallization, respectively. The purified region was identified from the macroscopic segregation morphology described below.

To evaluate the macroscopic segregation of primary Mg_2Si after fractional crystallization, the solidified samples were vertically sectioned through the central axis, ground, and polished. Representative Si-depleted Al—Mg and Mg_2Si-rich regions were identified by X-ray diffraction (XRD, Bruker AXS D8 Advance) using Cu Kα radiation. Microstructures and phase distributions were characterized by optical microscopy (OM, KEYENCE VHX-6000) and scanning electron microscopy (SEM, FEI Helios NanoLab G3 CX) equipped with energy-dispersive X-ray spectroscopy (EDS). SEM observations were performed in secondary electron (SE) and backscattered electron (BSE) modes to examine phase morphology and compositional contrast, respectively. Local phase compositions and elemental distributions were analyzed by EDS point and map analysis. The area fractions of the Si-depleted Al—Mg region and the primary Mg_2Si-rich layer were quantified from longitudinal cross-sectional images of the solidified samples by ImageJ software. The two regions were identified based on grayscale contrast and macroscopic segregation morphology, followed by thresholding and binarization. The area fraction of each region was calculated by dividing the corresponding region area by the effective cross-sectional area, with the shrinkage cavity excluded from the analysis.

3. Results and discussion

3.1. Thermochemical analysis

The solidification behavior of Al-9%Si alloy with different Mg addition levels was evaluated using FactSage 8.3, where the Mg addition level was defined as the mass percentage of added Mg to the initial Al-9%Si alloy, ranging from 0 to 50 wt%. Fig. 2(a) summarizes the calculated fractions of primary Mg_2Si and eutectic Mg_2Si, the Mg and Si contents remaining in the residual liquid alloy after hypothetical separation of primary Mg_2Si, and the corresponding theoretical Si removal efficiency. In the present analysis, eutectic Mg_2Si was regarded as practically non-separable because it precipitates cooperatively with α-Al or with α-Al and other phases, and is therefore may entrapped within the interdendritic and eutectic network. In contrast, primary Mg_2Si precipitates as a discrete first-solid phase and is thus considered the potentially separable Si-bearing phase. Accordingly, the theoretical Si removal efficiency was estimated under an idealized assumption that all primary Mg_2Si can be completely removed whereas eutectic Mg_2Si

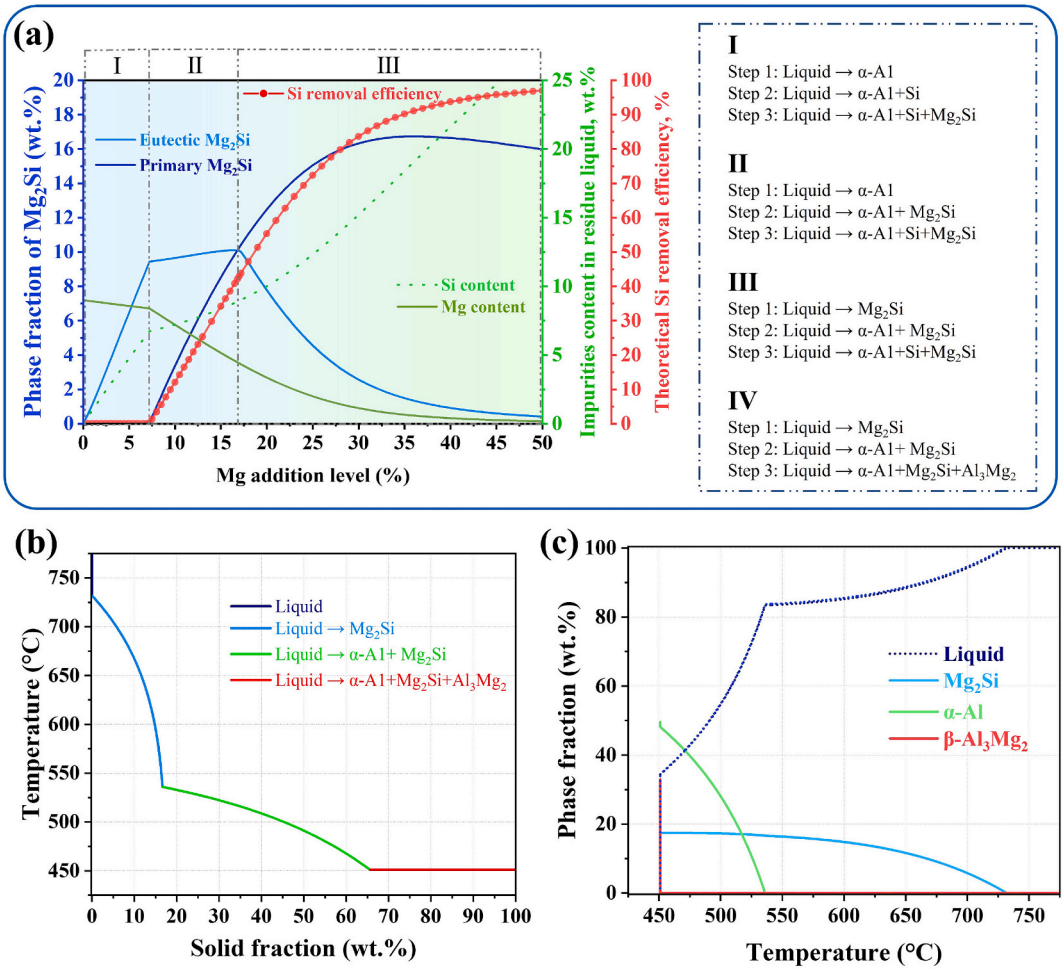


Fig. 2. Thermochemical results for Al-9%Si alloys with Mg addition by FactSage 8.3: (a) the influence of Mg addition level on Mg_2Si phase fractions, the Si and Mg content in the residual liquid, and theoretical Si removal efficiency; (b) Scheil-Gulliver solidification path of the alloy with 40% Mg addition relative to the initial Al-9%Si alloy mass; and (c) evolution of phase-fraction with temperature during solidification of the selected 40% Mg-added alloy.

remains in the alloy, which represents the maximum theoretical Si removal efficiency under the present separation criterion. The theoretical Si removal efficiency ($\eta_{T,Si}$) was calculated as:

$$\eta_{T,Si} = \frac{C_0 - C_L}{C_0} \times 100\% \quad (2)$$

where C_0 is the Si content (wt%) in the initial Al-Si-Mg alloy, and C_L is the calculated Si content (wt%) in the residual liquid after complete precipitation of primary Mg_2Si.

As shown in Fig. 2(a), when the Mg addition was below 7.2% (Regions I and II), no primary Mg_2Si was predicted to form. In this range, Mg mainly converted eutectic Si into eutectic Mg_2Si during the later stages of solidification, leading to a rapid increase in the eutectic Mg_2Si fraction. However, because this Mg_2Si remained associated with the eutectic and interdendritic structure, the theoretical separable Si fraction remained limited. When the Mg addition increased to 7.2–17.2% (Region III), primary Mg_2Si began to precipitate at the initial stage of solidification, and its fraction increased rapidly with increasing Mg content. This marks the onset of a thermochemically favorable regime for selective Si extraction, because Si is progressively transferred from non-separable eutectic products into a potentially separable primary intermetallic phase. When the Mg addition exceeded 17.2% (Region IV), the eutectic Si disappeared completely and the excess Mg precipitates as β-Al_3Mg_2 in the final solidification. In this range, the fraction of primary Mg_2Si first increased and then slightly decreased with further Mg addition, whereas the fraction of eutectic Mg_2Si decreased markedly. As a result, the theoretical Si removal efficiency continued to increase. Nevertheless, once the Mg addition exceeded approximately 40%, the increment in Si removal became marginal, although the Mg content remaining in the residual liquid continued to rise substantially. This would increase the downstream burden for Mg removal during the subsequent vacuum treatment. Therefore, 40% Mg was selected as a practical compromise between maximizing theoretical Si extraction and limiting the residual Mg level prior to vacuum refining. At this composition, the residual liquid alloy contained 21.63% Mg and 0.40% Si, corresponding to a theoretical Si removal efficiency of 93.7%.

To further clarify the temperature-dependent phase evolution of the Al-9%Si alloy with 40% Mg addition, the Scheil-Gulliver solidification path and the corresponding phase-fraction evolution are shown in Fig. 2 (b) and 2(c), respectively. These results provide the thermochemical basis for selecting the experimental temperature window. Primary Mg_2Si begins to precipitate at 731.8 °C. During cooling from 731.8 to 535.9 °C, 16.64% primary Mg_2Si is formed, indicating that a substantial fraction of Si is immobilized in a separable primary phase before the onset of extensive α-Al solidification. Upon further cooling to 535.9–451.0 °C, the alloy enters the second solidification stage, in which α-Al precipitates together with a small amount of eutectic Mg_2Si. In this stage, 48.13% α-Al and 0.85% eutectic Mg_2Si are formed. When the temperature reaches 451.0 °C, the remaining liquid solidifies under isothermal condition, generating 32.86% β-Al_3Mg_2 together with minor amounts of α-Al (0.07%) and eutectic Mg_2Si (1.45%).

The above thermochemical calculations and analyses not only clarify the phase evolution in the Al-9%Si with different Mg level, but also provide guidance for selecting the 40% Mg addition and the experimental temperature window for primary Mg_2Si formation and separation in the subsequent Mg-assisted electromagnetic fractional crystallization experiments.

3.2. Mg-assisted electromagnetic fractional crystallization

3.2.1. Macrostructural evolution and phase constitution

To elucidate the Mg-assisted electromagnetic fractional crystallization behavior of the Al-Si-Mg alloy, the separation and redistribution of primary Mg_2Si were systematically investigated under three different solidification modes: natural cooling without electromagnetic-field application, delayed electromagnetic-field treatment after completion of primary Mg_2Si precipitation, and continuous electromagnetic-field application during the primary Mg_2Si precipitation stage. The first two modes served as reference conditions, whereas the third mode represents the Mg-assisted electromagnetic fractional crystallization process proposed in this work. The corresponding vertical cross-sectional macrographs are presented in Fig. 3, which reveal the macroscopic distribution of the primary Mg_2Si-rich regions and the Mg_2Si-depleted purified alloy regions. Given the nominally axisymmetric geometry of the sample and processing configuration, the longitudinal section was assumed to provide an approximate representation of the overall segregation morphology. To correlate the macrosegregation behavior with phase constitution, XRD analysis was further conducted on representative primary Mg_2Si-enriched regions and Mg_2Si-depleted regions selected from each sample, as presented in Fig. 4.

For the sample solidified under natural cooling without electromagnetic-field application (denoted as #Without EM), a distinct macrosegregation of the black dendritic intermetallic phase was observed in the upper part of the sample and in the peripheral region adjacent to the crucible wall, as shown in Fig. 3(a). As shown in Figs. 4 (a) and 4(b), Mg_2Si diffraction peaks were detected in the top region of the #Without EM sample but were absent in the bottom region. Since the coarse black dendritic intermetallics were observed only in the Mg_2Si-containing region, they can be identified as Mg_2Si phase. FactSage calculation indicates that primary Mg_2Si precipitates from the Al-6.43% Si-28.57%Mg melt during the initial solidification stage. Combined with the predicted precipitation sequence and our previous identification of coarse dendritic Mg_2Si as primary Mg_2Si in Mg-assisted fractional crystallization [36], the coarse dendritic Mg_2Si phase enriched in the upper region can be assigned to primary Mg_2Si rather than eutectic Mg_2Si. By contrast, the bottom-central region shows no obvious Mg_2Si diffraction peaks and is dominated by Al and β-Al_3Mg_2 phase, as revealed by the XRD pattern in Fig. 4(b). This indicates that this region is depleted in primary Mg_2Si and corresponds to the low-Si purified Al alloy region, which can be regarded as the Si-removed product obtained after Mg-assisted fractional crystallization. Without the electromagnetic field, the separation of primary Mg_2Si is mainly driven by buoyancy, as the Mg_2Si density (1.99 g/cm^3 [43]) is lower than the Al melt, leading to its accumulation in the upper part of the sample. Meanwhile, the peripheral melt adjacent to the crucible wall experiences a relatively lower temperature during natural cooling, which likely facilitates heterogeneous nucleation and dendritic growth of primary Mg_2Si in this region. Consequently, primary Mg_2Si is mainly enriched in the top and peripheral regions, while the Mg_2Si-depleted region is restricted to the lower-central part of the ingot. Area analysis by ImageJ software further shows that the area fraction of the bottom Mg_2Si-depleted region in the #Without EM sample is only 17.8%, indicating a low recoverable purified fraction of the alloy under natural cooling conditions.

The cross-sectional macrographs of the samples subjected to delayed electromagnetic-field treatment after the completion of primary Mg_2Si precipitation are shown in Fig. 3(b) and (c). As shown in Fig. 3(b), for the sample treated at an AC current intensity of 530 A for 90 s after the complete precipitation of primary Mg_2Si, denoted as #530 A-90s, no obvious displacement or further aggregation of the coarse Mg_2Si dendrites was observed. Even when the treatment time was extended to 10 min at an AC current intensity of 430 A, as shown in Fig. 3(c), the Mg_2Si-rich region remained mainly distributed in the upper and peripheral regions of the #430 A-10 min sample, while the Mg_2Si-depleted region at the bottom remained narrow. The XRD patterns in Fig. 4(a) and (b) further reveal the phase constitution of the Mg_2Si-enriched and Mg_2Si-depleted regions in the #Without EM, #530 A-90s, and #430 A-10 min samples. The intermetallic-enriched regions exhibit intense Mg_2Si diffraction peaks, confirming the accumulation of Mg_2Si dendrites. Nevertheless, Al and β-Al_3Mg_2 peaks are also present, indicating that a considerable amount of Al—Mg matrix is retained within the interdendritic spaces of the coarse Mg_2Si network. In contrast, the

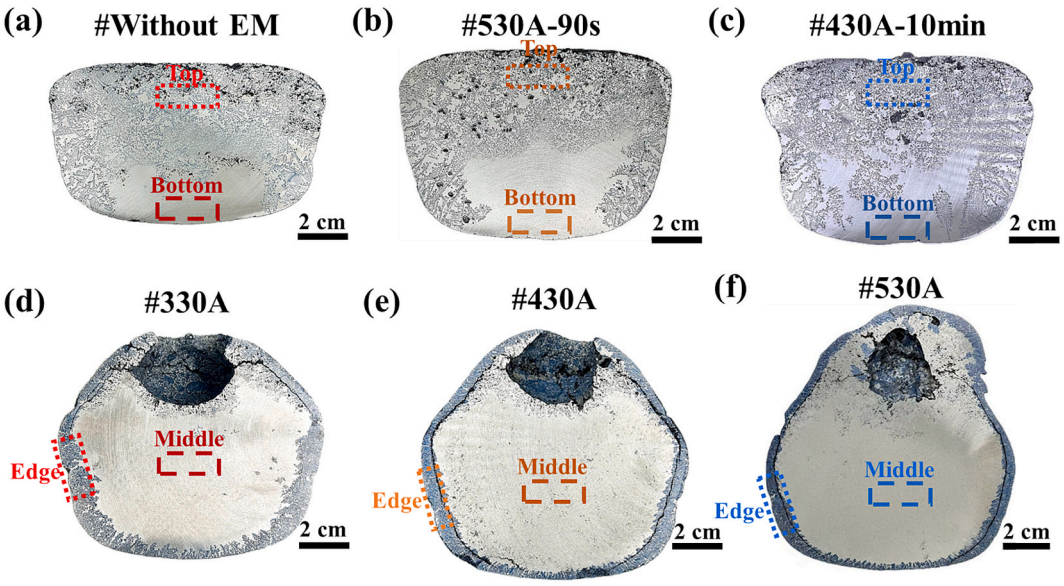


Fig. 3. Representative vertical cross-sections of samples obtained under different experimental conditions: (a) natural cooling without electromagnetic-field application; delayed electromagnetic-field treatment after primary Mg_2Si precipitation at current intensities of (b) 530 A for 90 s, and (c) 430 A for 10 min; and continuous electromagnetic-field application during primary Mg_2Si precipitation at current intensities of (d) 330 A, (e) 430 A, and (f) 530 A.

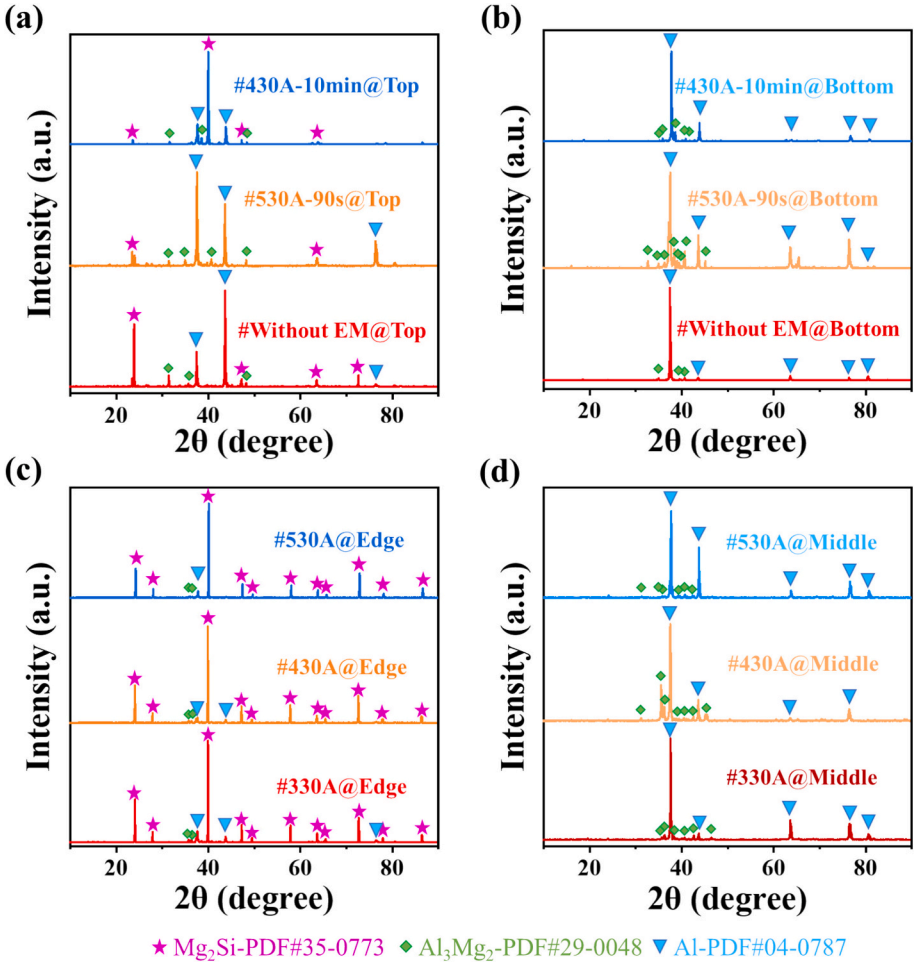


Fig. 4. XRD patterns of selected regions in the samples obtained under different experimental conditions: (a) primary Mg_2Si-enriched top region and (b) primary Mg_2Si-depleted bottom purified region of the #Without EM, #530 A-90s, and #430 A-10 min samples; (c) primary Mg_2Si-enriched edge region and (d) primary Mg_2Si-depleted middle purified region of the #330 A, #430 A, and #530 A samples.

purified bottom regions are dominated by Al and β-Al_3Mg_2, with negligible Mg_2Si diffraction peaks, confirming their primary Mg_2Si-depleted character. This limited redistribution indicates that electromagnetic-field treatment is ineffective once primary Mg_2Si has grown into coarse dendritic structures. At this stage, Mg_2Si is no longer present as mobile fine particles [44], but as coarse, rigid dendritic crystals or partially interconnected networks. Since the Lorentz force generated by the alternating electromagnetic field mainly drives convection in the conductive melt, the induced fluid shear in this study is insufficient to break or rearrange the pre-existing Mg_2Si dendritic network [45,46]. In addition, the increased solid fraction after primary Mg_2Si precipitation raises the effective viscosity of the slurry and suppresses long-range particle transport [47]. Therefore, the shape factor, high hydrodynamic drag and mechanical interlocking strongly restrict their movement [48,49], making it difficult to further improve the yield of the low-Si alloy.

In contrast, a markedly different macrosegregation behavior was observed when the electromagnetic field was continuously applied during the primary Mg_2Si precipitation stage. As shown in Fig. 3(d-f), primary Mg_2Si was no longer loosely concentrated at the top region, but was strongly concentrated along the outer edge of the sample, where it formed a highly compact, Mg_2Si-dominated peripheral layer with only limited entrapped matrix alloy. The corresponding XRD patterns in Fig. 4(c) confirm that the edge regions of the #330 A, #430 A, and #530 A samples are dominated by Mg_2Si phase, with only very weak Al and β-Al_3Mg_2 peaks. The dendritic Mg_2Si phase grows from the edge toward the interior of the sample, while a large Mg_2Si-depleted region was retained in the middle of sample. As shown in Fig. 4(d), the middle purification regions mainly consist of Al and β-Al_3Mg_2, while the Mg_2Si peaks are extremely weak or nearly below the XRD detection limit. This indicates that continuous electromagnetic field-assisted fractional crystallization can efficiently concentrate primary Mg_2Si at the edge of sample, thereby greatly expanding the central Mg_2Si-depleted purified region and substantially improving the effective yield of the low-Si alloy. These observations indicate that efficient phase separation requires Mg_2Si crystals to remain mobile during solidification. Therefore, the application timing of the electromagnetic field is critical. The EM field should be applied during primary Mg_2Si precipitation, when Mg_2Si particles are still nucleating, growing, and moving in the melt, rather than after the dendritic Mg_2Si network has already formed.

The effect of electromagnetic-field intensity can also be observed from the macrostructures in Fig. 3(d-f). With increasing current intensity from 330 A to 530 A, the Mg_2Si-enriched peripheral layer becomes thinner and more compact, while the middle Mg_2Si-depleted purified region expands. To semi-quantitatively evaluate this change, the area fraction of the central purified region was measured from the cross-sectional images using ImageJ. The purified-region area fractions of the #330 A, #430 A, and #530 A samples were calculated to be 71.15%, 78.30%, and 79.50%, respectively. This trend indicates that a stronger alternating electromagnetic field suggests enhanced migration and particle accumulation, likely accompanied by increased collision and agglomeration, and consequently enrichment of primary Mg_2Si. In these experiments, electromagnetic field intensity was coupled with the cooling rate of melt. The average cooling rates over 750–535 °C were 3.79, 2.17, and 1.95 °C/min under continuous EM treatment at 330, 430, and 530 A, respectively, compared with approximately 6–7 °C/min without EM. Slower cooling allows more time for primary Mg_2Si growth, coarsening, and flotation. To evaluate its influence, an additional solidification experiment was performed in a resistance furnace without an applied electromagnetic field at an average cooling rate of approximately 2 °C/min, comparable to those of the #430 A and #530 A samples. In this control sample, primary Mg_2Si was concentrated mainly in the upper region, and the purified-region area fraction was substantially smaller than in the continuously EM-treated samples (Fig. S1). Thus, solidification without EM at a similarly low average cooling rate did not reproduce the compact peripheral enrichment observed under continuous EM treatment. This comparison indicates that continuous EM field plays a critical role in the accumulation and compact packing of primary Mg_2Si near the crucible wall. During continuous electromagnetic treatment at 430 A, temperature measurements at the locations shown in Fig. S2 revealed that the melt center had the highest temperature. The top and bottom regions of the melt were approximately 2–3 °C cooler than the center, whereas the melt adjacent to the crucible wall was approximately 23 °C cooler. The enhanced Lorentz-force-driven melt convection and electromagnetic expulsive (extrusion) force may facilitate the transport of newly precipitated Mg_2Si toward the colder crucible-wall region, where the particles further accumulate and grow [50]. Consequently, a stronger electromagnetic field improves the spatial separation between the Mg_2Si-rich region and the Mg_2Si-depleted Al—Mg alloy region, thereby increasing the effective yield of the purified alloy. It should also be noted that a cavity is formed near the top of the continuously treated samples, especially at higher current intensities. This cavity is most likely attributed to solidification shrinkage and insufficient feeding during the final stage of solidification [51]. In addition, the apparent increase in sample height with increasing current intensity is mainly associated with electromagnetic field induced free-surface deformation [52]. A stronger alternating current is expected to enhance the Lorentz-force density and the resulting electromagnetic pressure acting on the conductive melt, which disturbs the hydrostatic balance of the free surface [53]. Consequently, the melt may form a dome-shaped meniscus or upward bulging profile prior to complete solidification, resulting in an apparent increase in the final sample height.

3.2.2. *Chemical composition evolution and Si removal performance*

Chemical composition analysis was performed on the primary Mg_2Si-enriched and Mg_2Si-depleted regions of samples to quantitatively evaluate the redistribution of Mg and Si under different solidification conditions. The removal efficiency was calculated relative to the initial Al-Si-Mg alloy composition, with the initial Mg and Si contents being 28.54 wt% and 6.45 wt%, respectively.

For the samples solidified without electromagnetic-field application or subjected to delayed electromagnetic-field treatment after primary Mg_2Si precipitation, the Mg and Si distributions are shown in Fig. 5 (a) and (b). In the #Without EM sample, the Mg content was 39.25 wt% in the top Mg_2Si-enriched region, and decreased to 21.55 wt% in the bottom purified region corresponding to a Mg removal efficiency of 24.50%. Similar values were obtained for the #530 A-90s and #430 A-10 min samples, where the Mg contents in the top and bottom regions remained close to those of the #Without EM sample. This indicates that applying the electromagnetic field after primary Mg_2Si precipitation does not significantly alter the enrichment of primary Mg_2Si phases. Si followed a redistribution trend similar to that of Mg in the #Without EM, #530 A-90s, and #430 A-10 min samples. As shown in Fig. 5(b), the Si content in the top Mg_2Si-enriched region of the #Without EM sample reached 15.58 wt%, while that in the bottom purified region decreased from the initial 6.45 wt% to 0.406 wt%, corresponding to a Si removal efficiency of 93.71%. The purified bottom regions of the #530 A-90s and #430 A-10 min samples showed comparable Si removal efficiencies of 93.64% and 93.75%, respectively. These results demonstrate that Mg addition enables efficient Si removal by converting Si into separable primary Mg_2Si. However, the comparable Mg and Si contents in the top Mg_2Si-enriched regions of the three samples indicate that delayed electromagnetic-field treatment does not further increase Mg_2Si enrichment once coarse primary Mg_2Si dendrites have formed, and thus fails to effectively improve the yield of the low-Si Al—Mg alloy product.

The effect of continuous electromagnetic-field application during primary Mg_2Si precipitation on the chemical redistribution between the primary Mg_2Si-enriched edge region and the Mg_2Si-depleted central purified region is shown in Fig. 5(c) and (d). Compared with the Mg_2Si-enriched top region of the #Without EM sample, the edge regions of the continuously EM treated samples exhibited much higher Mg and Si

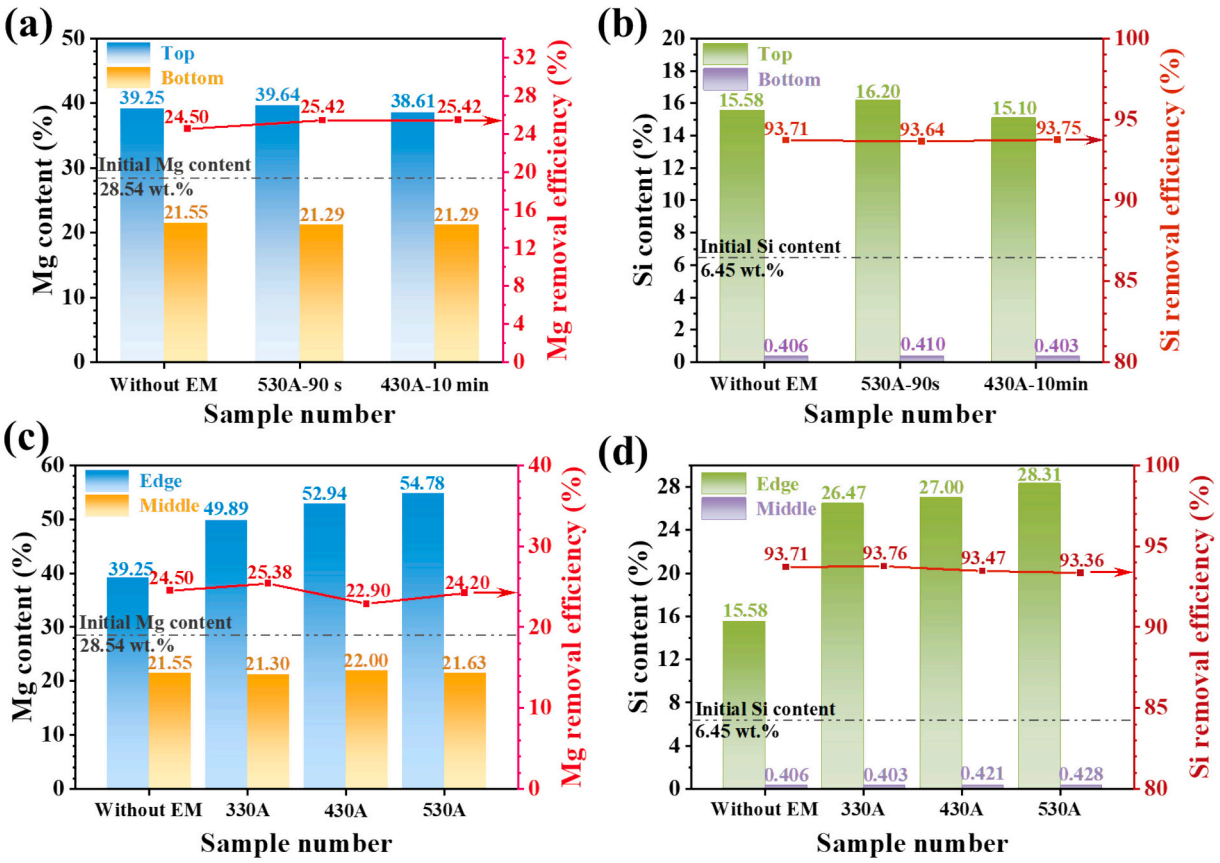


Fig. 5. Chemical compositions and removal efficiencies of Mg and Si during Mg-assisted electromagnetic fractional crystallization: (a) Mg contents in the top Mg_2Si-enriched regions and bottom purified regions of the #Without EM, #530 A-90s, and #430 A-10 min samples and Mg removal efficiencies in the purified regions; (b) corresponding Si contents and Si removal efficiencies; (c) Mg contents in the Mg_2Si-enriched regions and purified regions of the #Without EM, #330 A, #430 A, and #530 A samples and Mg removal efficiencies in the purified regions; and (d) corresponding Si contents and Si removal efficiency.

contents, demonstrating a markedly enhanced enrichment of primary Mg_2Si under continuous electromagnetic-field application. Specifically, the Mg and Si contents increased from 39.25 wt% and 15.58 wt% in the top region of the #Without EM sample to 49.89 wt% and 26.47 wt% in the edge region of the #330 A sample, respectively. This indicates that continuous electromagnetic-field application transformed the relatively loose Mg_2Si accumulation obtained under natural cooling or delayed electromagnetic field treatment into a much more compact Mg_2Si-rich peripheral layer. With increasing current intensity from 330 A to 530 A, the Mg content in the edge region further increased from 49.89 wt% to 54.78 wt%, while the Si content increased from 26.47 wt% to 28.31 wt %. This simultaneous increase in Mg and Si content indicates that a stronger electromagnetic field further correlates with greater concentration and compaction of primary Mg_2Si at the sample edge, which is consistent with the thinner and denser Mg_2Si-rich edge layer observed in Fig. 3(d-f). The Mg/Si mass ratio in the edge region of the #530 A sample is 1.94, which is slightly higher than the stoichiometric value of Mg_2Si (1.73), suggesting that the edge layer is dominated by Mg_2Si but still contains a small amount of entrapped Al—Mg matrix. This interpretation is consistent with the weak α-Al and β-Al_3Mg_2 diffraction peaks detected in the XRD patterns in Fig. 4(c).

In contrast, the central regions of the #330 A, #430 A, and #530 A samples maintained low Si contents of 0.403 wt%, 0.421 wt%, and 0.428 wt%, respectively, corresponding to Si removal efficiencies of 93.76%, 93.47%, and 93.36%. These values agree well with the FactSage-predicted residual liquid composition of the Al-9%Si with 40% Mg addition level, in which the purified Al—Mg alloy after primary Mg_2Si separation contains approximately 0.40 wt% Si and 21.63 wt % Mg, corresponding to a theoretical Si removal efficiency of 93.7%. The measured Mg contents in the central purified regions, ranging from 21.30 wt% to 22.00 wt%, also support that these regions correspond to the purified Al—Mg residual alloy predicted by thermochemical calculation. Therefore, Mg-assisted electromagnetic fractional crystallization reduces the Si concentration in the purified alloy close to the thermochemically predicted residual Si concentration while simultaneously controlling the spatial redistribution of primary Mg_2Si. By compacting primary Mg_2Si at the sample edge, the process substantially enlarges the central low-Si alloy region without sacrificing its purification level, thereby improving the effective yield of the purified product. That means, unlike conventional process optimization, the electromagnetic field does not improve the purification degree itself; instead, it enlarges the volume fraction of alloy reaching the same thermochemical purification level. These represent the key advantage of the proposed Mg-assisted electromagnetic fractional crystallization strategy.

3.2.3. *Microstructural characterization*

SEM-EDS analysis was further carried out on the primary Mg_2Si-enriched regions and the primary Mg_2Si-depleted purified regions of the #Without EM, #330 A, #430 A, and #530 A samples. SEM was used to examine the local microstructural features, phase morphology, particle size, and spatial distribution of the constituent phases, while EDS was employed to determine their chemical compositions and elemental distribution characteristics. These analyses provide microstructural evidence for clarifying the mechanism by which continuous electromagnetic-field application governs the redistribution, enrichment behavior, and morphological evolution of primary Mg_2Si during Mg-assisted fractional crystallization.

Fig. 6 shows the SEM-EDS characterization of the Mg_2Si-enriched top

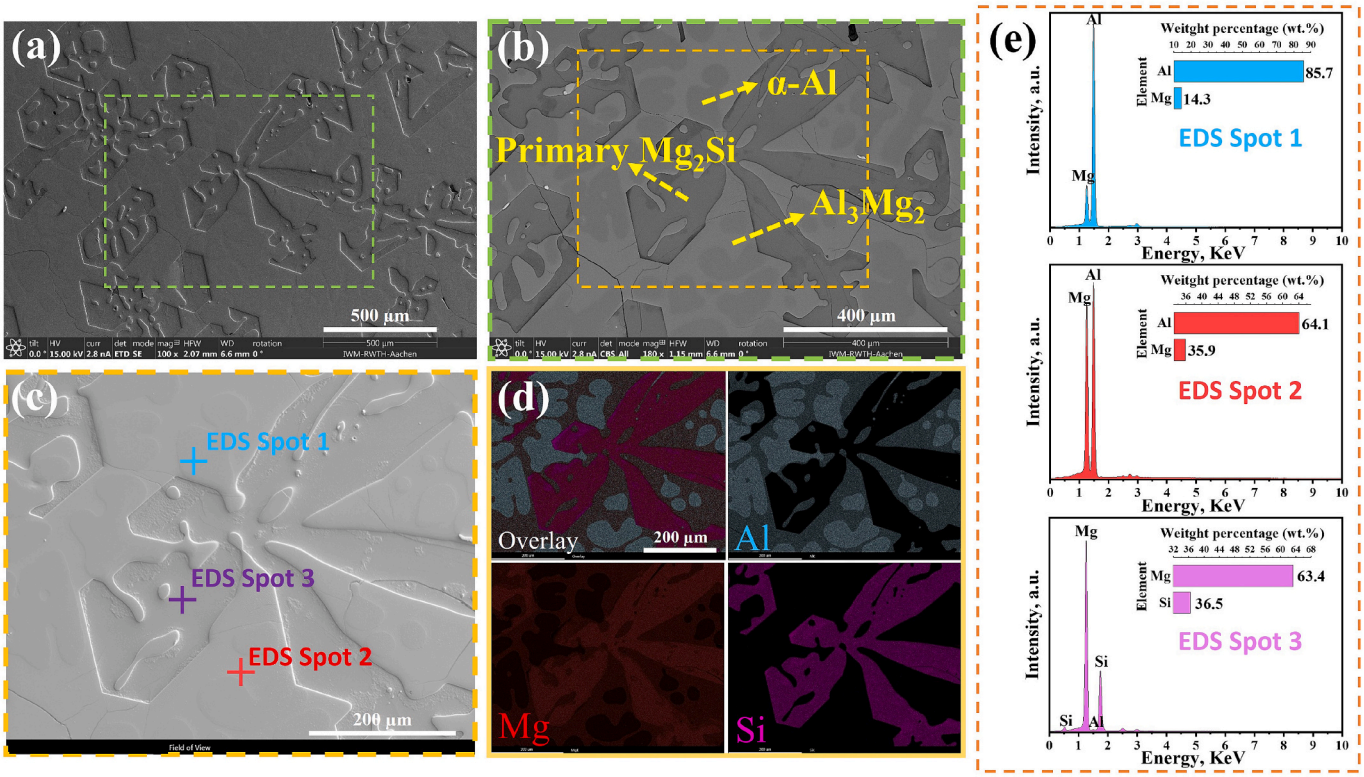


Fig. 6. Microstructural and compositional characterization of the Mg_2Si-enriched top region of the #Without EM sample: (a) low-magnification SE-SEM image; (b) enlarged BSE-SEM image; (c) EDS spot-analysis positions; (d) corresponding EDS elemental mappings of Al, Mg, and Si from the area shown in (c); and (e) EDS spot spectra and chemical composition of the selected phases.

region of the #Without EM sample. Three main phases can be distinguished: coarse dendritic/faceted phase [54,55], rounded dendritic or island-like phase [56], and irregular interdendritic phase. EDS analysis in Fig. 6(e) shows that the coarse dendritic particle contains approximately 63.4 wt% Mg and 36.5 wt% Si, close to the stoichiometric composition of Mg_2Si. Combined with its large size, coarse dendritic crystals with locally faceted branches, and the thermochemical prediction that Mg_2Si first precipitates as the primary phase during the initial solidification stage, this phase can be identified as primary Mg_2Si rather than eutectic Mg_2Si [57]. The rounded dendrite phase is mainly distributed in the interdendritic spaces between the primary Mg_2Si crystals. EDS analysis indicates that it is an Al-rich phase containing 14.3 wt% Mg, corresponding to a Mg-containing α-Al solid phase. Its smooth and rounded morphology, without pronounced faceted intermetallic features, suggests that it formed from the residual Al—Mg melt trapped between the growing primary Mg_2Si dendrites. The dissolved Mg in α-Al can expand the FCC Al lattice, explaining the slight shift of the α-Al peaks toward lower 2θ angles relative to the standard Al PDF card, as shown in Fig. 4(a) [58]. The irregular interdendritic phase, with an EDS composition of approximately 64.1 wt% Al and 35.9 wt% Mg, was identified as β-Al_3Mg_2. Its semi-continuous distribution between the round α-Al regions and primary Mg_2Si crystals suggests that it formed from the Mg-rich residual liquid through a divorced eutectic-type solidification during the final solidification stage [59]. This interpretation is consistent with the FactSage precipitation sequence, in which β-Al_3Mg_2 precipitates in the final solidification stage after the formation of primary Mg_2Si and a substantial α-Al. These observations demonstrate that the Mg_2Si-enriched top region of the #Without EM sample is not a compact Mg_2Si layer. Instead, it consists of loosely accumulated coarse primary Mg_2Si dendrites with a considerable amount of entrapped Al—Mg matrix. Under natural cooling, primary Mg_2Si nucleates at multiple locally undercooled sites within the melt and grows independently into coarse faceted dendrites [54]. In the absence of electromagnetically induced convection and sufficient driving forces, there is insufficient particle migration, collision, and compaction [60]. Therefore, primary Mg_2Si separation is governed mainly by buoyancy-driven flotation in this case. The floating Mg_2Si dendrites accumulate loosely in the upper region, while residual Al—Mg liquid remains in the interdendritic spaces and subsequently solidifies into α-Al and β-Al_3Mg_2. This explains why Al and β-Al_3Mg_2 diffraction peaks are still detected in the Mg_2Si-enriched top region in Fig. 4(a).

Fig. 7 shows the microstructure of the primary Mg_2Si-depleted bottom region of the #Without EM sample. In this region, no coarse faceted primary Mg_2Si was observed. Instead, the microstructure consists mainly of rounded/cellular Al phase, irregular interdendritic Al_3Mg_2 phase, and a small amount of black Mg_2Si phase, which were primarily identified based on the chemical compositions obtained from EDS spot analysis and elemental mapping, as shown in Fig. 7(c-e). EDS analysis (Spot 1) confirms that the rounded dendritic phase is Mg-containing α-Al solid solution, with an Mg content of approximately 13.8 wt%. The black Mg_2Si constituent exhibits an irregular skeleton-like or Chinese-script-like morphology and is locally distributed in the interdendritic regions between α-Al and β-Al_3Mg_2. This morphology is clearly different from the coarse faceted morphology of primary Mg_2Si and is consistent with reported eutectic Mg_2Si morphologies in Al-Mg-Si-based alloys [61,62]. Thermochemical calculations show that, after the first solidification stage, the remaining liquid further solidifies through the precipitation of α-Al and a small amount of eutectic Mg_2Si, with calculated phase fractions of 48.13% and 0.85% relative to the whole alloy, respectively. In the final solidification stage, β-Al_3Mg_2 becomes the dominant residual phase, with a calculated phase fraction of 32.86%, accompanied by minor α-Al and eutectic Mg_2Si fractions of 0.07% and 1.45%, respectively. These calculated phase fractions are in reasonable agreement with the microstructural analysis, which shows abundant α-Al and β-Al_3Mg_2 phases and only a small fraction of eutectic Mg_2Si in the bottom purified region.

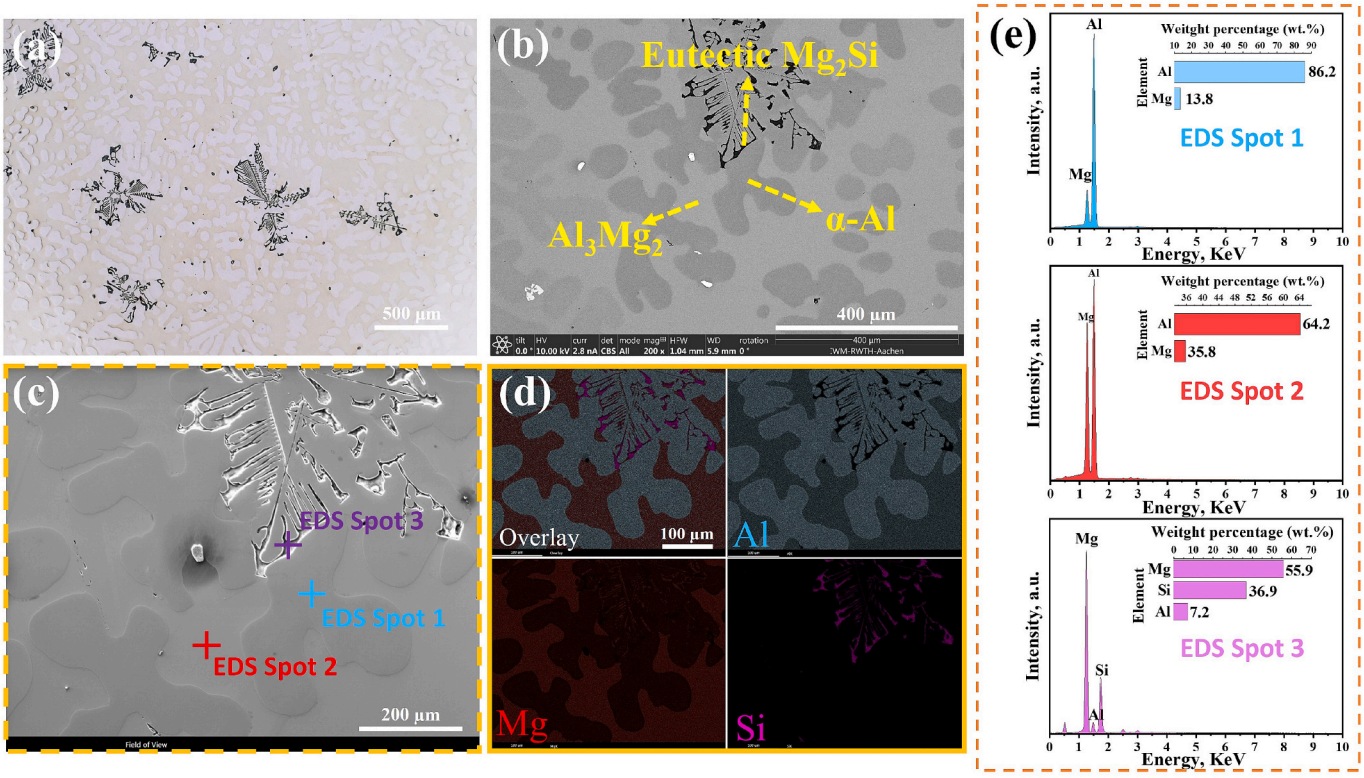


Fig. 7. Microstructural and compositional characterization of the primary Mg_2Si-depleted bottom region of the #Without EM sample: (a) optical micrograph; (b) BSE-SEM image; (c) EDS spot-analysis positions; (d) corresponding EDS elemental mappings of Al, Mg, and Si from the area shown in (c); and (e) EDS spectra and compositions of the selected phases.

Fig. 8 presents the microstructural and compositional characterization of the Mg_2Si-enriched edge region of the #330 A sample. In contrast to the #Without EM sample, where primary Mg_2Si accumulates loosely in the top region, continuous electromagnetic-field application during primary Mg_2Si precipitation promotes the formation of a compact Mg_2Si-rich peripheral layer at the sample edge. The dense blue phase observed in the optical micrograph in Fig. 8(a), corresponding to the coarse dendritic/faceted dark-grey phase in the BSE-SEM image in Fig. 8 (c) is identified as primary Mg_2Si, based on the EDS elemental mapping and spot analysis shown in Fig. 8(d)(e). Based on the EDS results, the grey constituent distributed between the primary Mg_2Si dendrites in Fig. 8(c) is identified as α-Al, showing a rounded cellular/island-like or rounded dendritic morphology. The light-grey irregular constituent is assigned to β-Al_3Mg_2. The remaining interdendritic regions contain only limited α-Al and β-Al_3Mg_2, indicating a much lower degree of matrix entrapment than in the #Without EM top region. The crack observed in the Mg_2Si-rich edge layer in Fig. 8(a) likely formed during cooling, as the thermal-contraction mismatch with the surrounding Al—Mg matrix generated local stresses within the intrinsically brittle Mg_2Si network [63,64]. Importantly, the formation of these interfacial cracking enabled mechanical separation of the Mg_2Si-rich outer shell from the purified Al—Mg core. Tapping was sufficient to detach the Mg_2Si-rich shell after the trials.

The microstructural differences of samples shown in Fig. 6 and Fig. 8 can be attributed to the coupled effects of electromagnetic-field-induced melt convection, force-assisted migration of primary Mg_2Si, and enhanced cooling near the sample periphery during Mg-assisted electromagnetic fractional crystallization. When the electromagnetic field is continuously applied during primary Mg_2Si precipitation, the Mg_2Si crystals remain mobile before forming a rigid interconnected dendritic network. During cooling, the melt adjacent to the crucible wall has a lower temperature than the central melt, resulting in greater local undercooling and thereby promoting the heterogeneous nucleation of primary Mg_2Si near the sample edge and its subsequent growth toward the melt interior. Meanwhile, Lorentz-force-driven melt convection enhances heat and solute transport at the Mg_2Si/melt interface, ensuring sufficient Mg and Si supply for continued Mg_2Si growth. In addition, due to the conductivity difference between Mg_2Si and the Al melt, the suspended Mg_2Si particles can also experience an electromagnetic expulsion force in electromagnetic field, which promotes their migration and accumulation toward the crucible wall in this study [44,65]. Therefore, the dense Mg_2Si-dominated edge layer is attributed to the coupled effects of peripheral cooling-induced nucleation, electromagnetic stirring-enhanced solute transport, and force-assisted migration and capture of primary Mg_2Si at the sample edge.

Fig. 9 shows the primary Mg_2Si-depleted middle region of the #330 A sample. Based on the EDS elemental mapping and spot analysis in Fig. 9 (c-e) together with the corresponding morphology, this region is mainly composed of rounded/cellular or dendritic α-Al, irregular β-Al_3Mg_2, and locally distributed residual eutectic Mg_2Si with a skeleton-like or Chinese-script-like morphology. The absence of coarse faceted primary Mg_2Si confirms that the continuous electromagnetic-field application markedly altered its spatial distribution, resulting in primary Mg_2Si depletion from the center and enrichment near the sample edge. Compared with the #Without EM bottom region, the residual eutectic Mg_2Si in the #330 A middle region appears finer and more dispersed. Because the electromagnetic field was switched off after primary Mg_2Si precipitation, this refinement should be regarded as a subsequent effect of the earlier electromagnetic-field-assisted redistribution rather than a direct effect during eutectic solidification. Specifically, the electromagnetic-field-induced melt convection promotes the migration of primary Mg_2Si toward the sample edge and enhances solute and temperature homogenization in the middle region, thereby suppressing local Si enrichment during the later solidification stage. Consequently, residual eutectic Mg_2Si forms as finer and more dispersed interdendritic constituents.

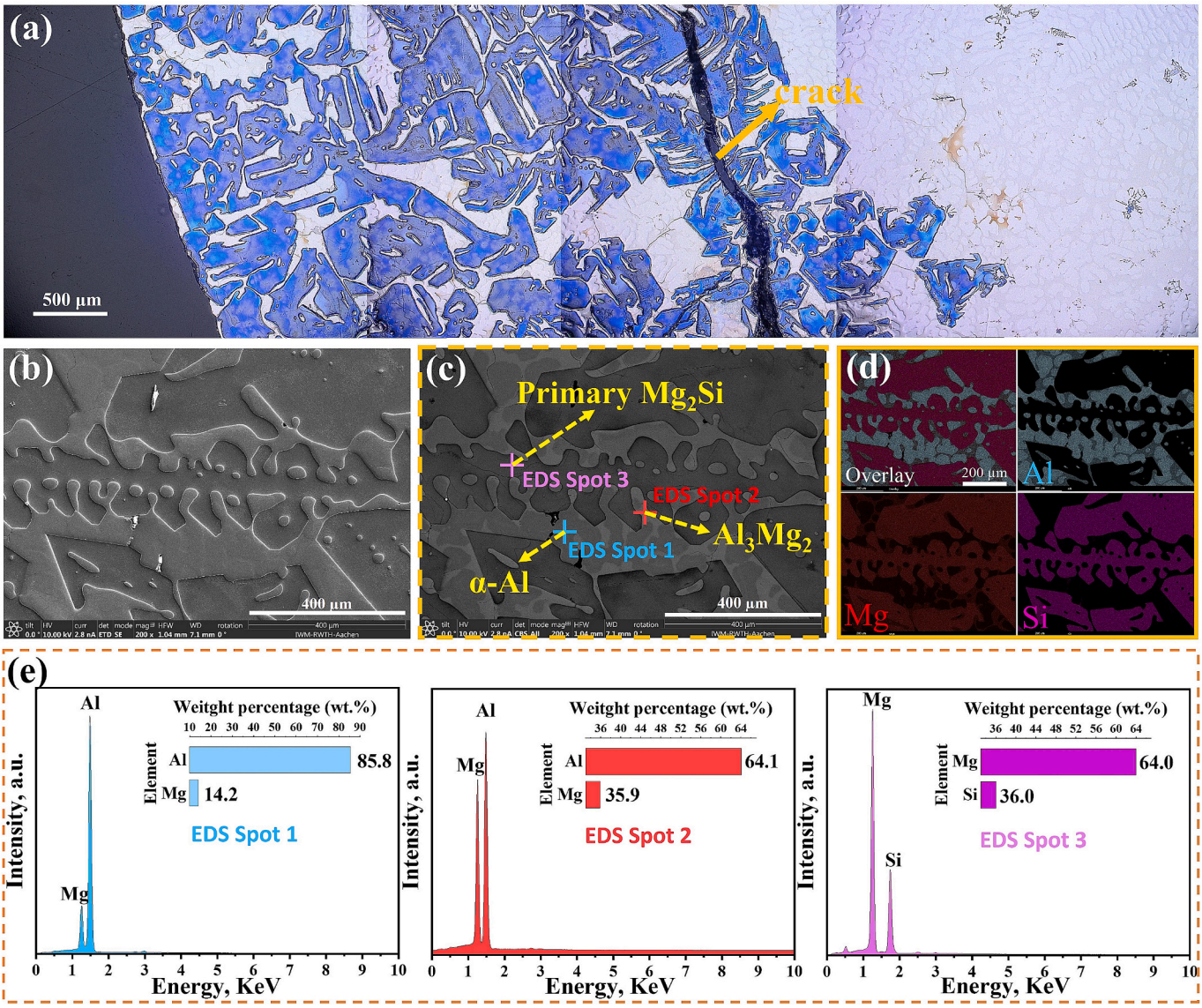


Fig. 8. Microstructural and compositional characterization of the Mg_2Si-enriched edge region of the #330 A sample: (a) optical micrograph; (b) SE-SEM image; (c) BSE-SEM image with EDS spot-analysis positions; (d) EDS elemental mappings of Al, Mg, and Si from the area shown in (c); and (e) EDS spectra and compositions of the selected phases.

Fig. 10 shows the microscopic optical images of sample #430 A. In the edge region, a large amount of primary Mg_2Si is enriched and forms a compact peripheral layer. Compared with the #330 A sample, the Mg_2Si-rich layer exhibits a higher apparent area fraction and denser packing of primary Mg_2Si, indicating that increasing the electromagnetic-field intensity correlates with more effective Mg_2Si accumulation and compaction. The primary Mg_2Si-depleted middle purified region shown in Fig. 10(b-d) exhibits a microstructure similar to that of the #330 A middle region, consisting mainly of α-Al and β-Al_3Mg_2 with only residual eutectic Mg_2Si. This again confirms that the main role of continuous electromagnetic-field application is to redistribute primary Mg_2Si into the peripheral layer, while leaving the central region as a primary Mg_2Si-depleted low-Si Al—Mg alloy.

Fig. 11 shows the Mg_2Si-enriched edge region of the #530 A sample, where primary Mg_2Si is more densely packed than in the edge region of #330 A and #430 A samples. A comparison of Figs. 8, 10, and 11 reveals that increasing electromagnetic-field intensity markedly reduces the amount of entrapped α-Al and β-Al_3Mg_2 between primary Mg_2Si dendrites. This suggests that a stronger electromagnetic field promotes more efficient migration, accumulation, and compaction of primary Mg_2Si to the sample edge. This provides microstructural support for the compositional results in Fig. 5(c, d), where the Mg and Si contents in the edge region increase with current intensity. In contrast, the middle region of the #530 A sample (Fig. 12) remains primary Mg_2Si-depleted and shows a phase constitution comparable to those of the #330 A and #430 A middle regions, consisting mainly of α-Al, β-Al_3Mg_2, and minor residual eutectic Mg_2Si. No significant differences in morphology, size, or distribution are observed among the middle regions under different electromagnetic-field intensities, suggesting that the field intensity primarily affects the edge enrichment and compaction of primary Mg_2Si rather than the microstructure of the central purified region.

3.3. *Integrated mechanism of upcycling via Mg-assisted electromagnetic fractional crystallization*

Based on the above thermochemical, macrostructural, chemical, and microstructural analyses, the integrated mechanism of Si removal from Al—Si scrap via Mg-assisted electromagnetic fractional crystallization is schematically illustrated in Fig. 13. The mechanism can be understood as a coupled process involving thermochemical phase transformation,

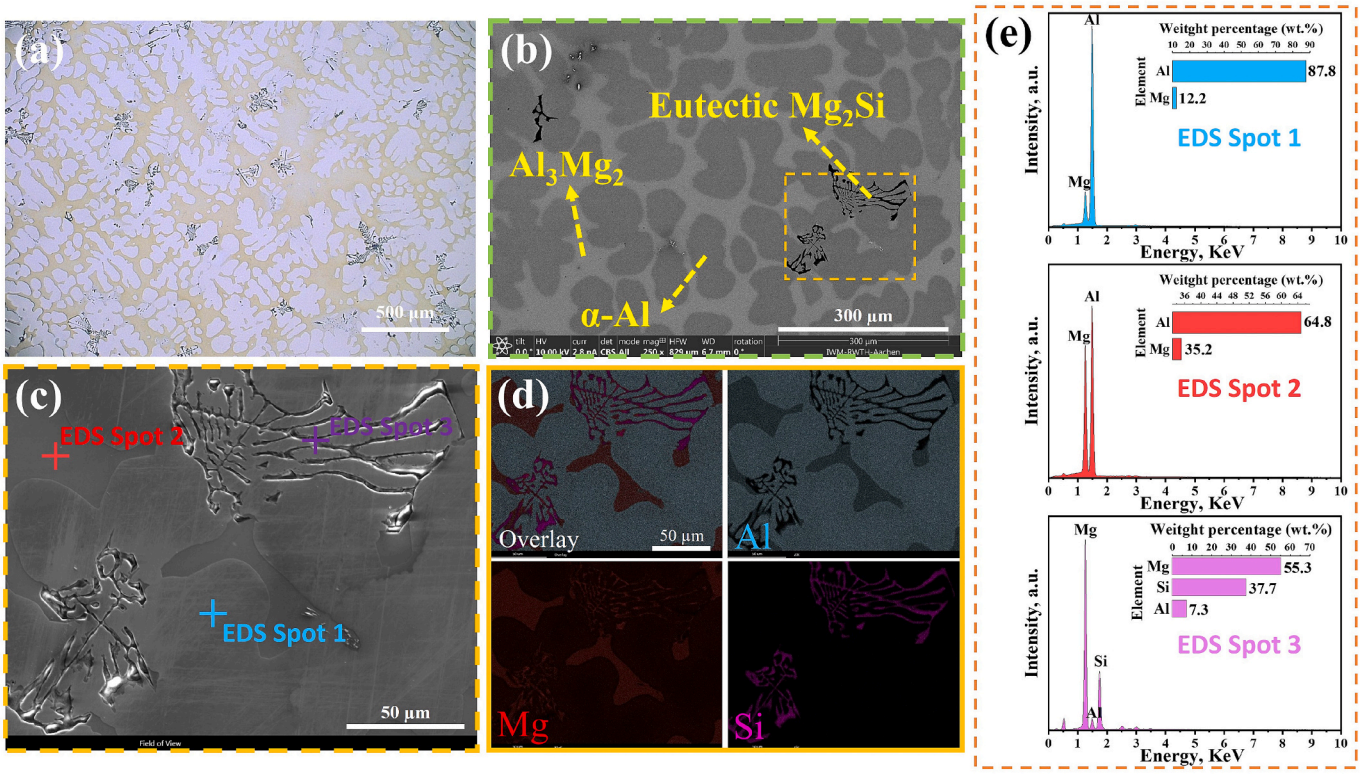


Fig. 9. Microstructural and compositional characterization of the Mg_2Si-depleted middle region of the #330 A sample: (a) optical micrograph; (b) BSE-SEM image; (c) enlarged SEM image with EDS spot-analysis positions; (d) EDS elemental mappings of Al, Mg, and Si from the area shown in (c); and (e) EDS spectra and compositions of the selected phases.

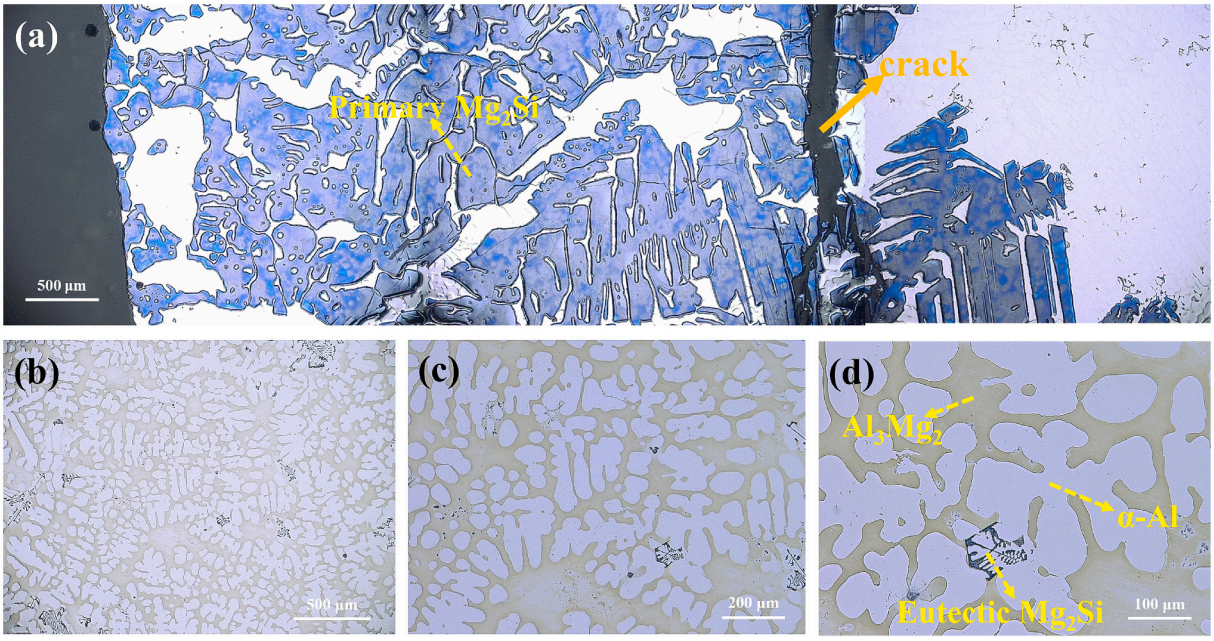


Fig. 10. Microstructural characterization of the #430 A sample: (a) optical micrograph of the primary Mg_2Si-enriched edge region; and (b-d) optical micrographs of the primary Mg_2Si-depleted middle purified region at different magnifications.

peripheral heterogeneous nucleation, electromagnetic-field-induced melt convection, electromagnetic-force-assisted particle migration, and interfacial growth of primary Mg_2Si.

In the first stage, a certain amount of Mg is introduced into the Al—Si scrap melt to form a chemically homogeneous Al-Si-Mg liquid. The essential role of Mg is to change the solidification pathway of Si. In conventional hypoeutectic Al—Si alloys, Si mainly precipitates as eutectic Si coupled with α-Al, making direct physical separation difficult. In contrast, after sufficient Mg addition, a large fraction of Si can be incorporated into primary Mg_2Si phase during the initial solidification

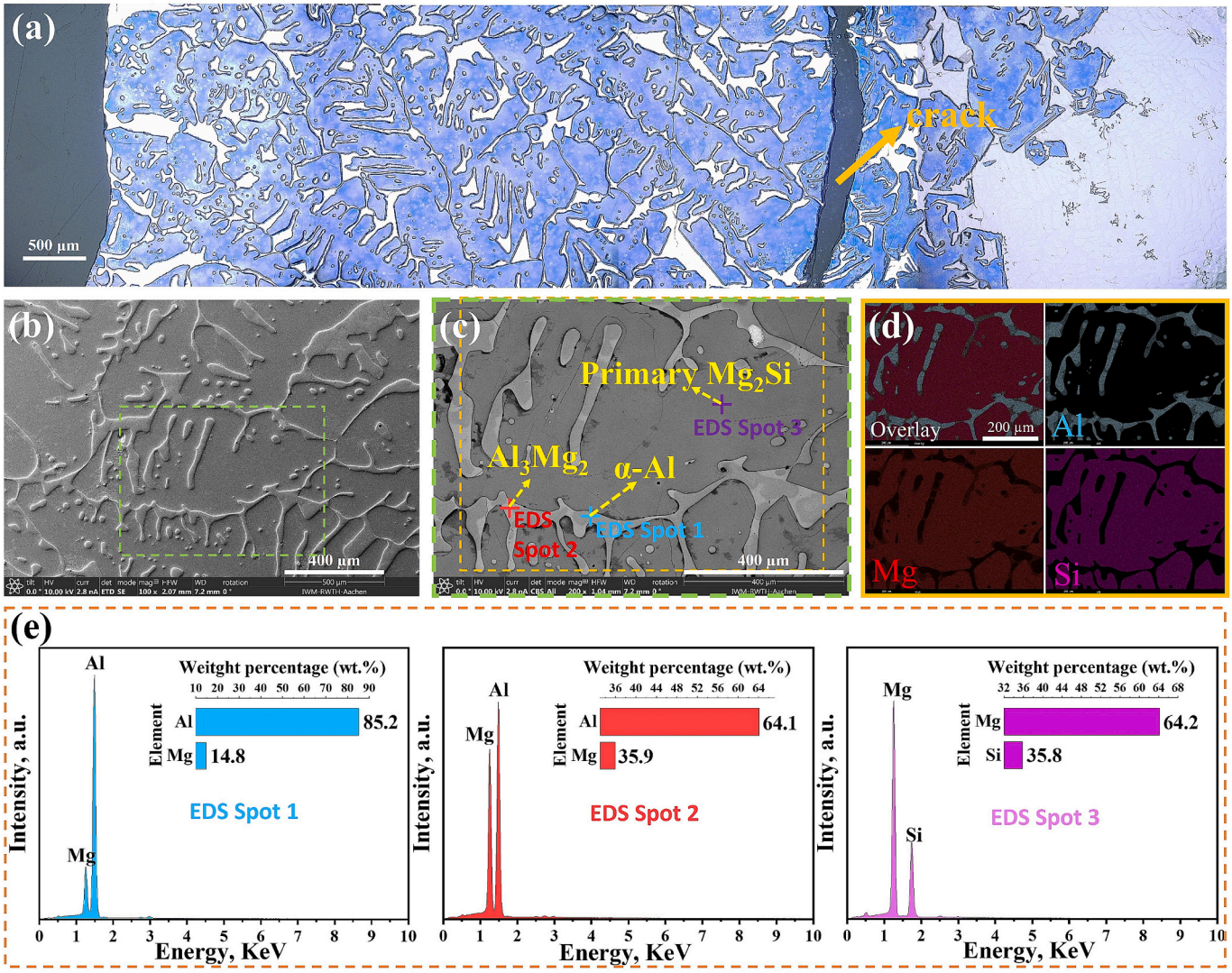


Fig. 11. Microstructural and compositional characterization of the Mg_2Si-enriched edge region of the #530 A sample: (a) optical micrograph; (b) SE-SEM image; (c) BSE-SEM image with EDS spot-analysis positions; (d) EDS elemental mappings of Al, Mg, and Si from the area shown in (c); and (e) EDS spectra and compositions of the selected phases.

stage. Therefore, Mg addition converts Si from a non-separable eutectic constituent into a separable primary intermetallic carrier phase. During the second stage, the electromagnetic field is continuously applied within the primary Mg_2Si precipitation window. As the melt cools, heat extraction through the crucible wall generates a radial thermal gradient, with a colder peripheral region and a hotter central region. The higher local undercooling near the crucible wall, together with the wall surface acting as a favorable heterogeneous nucleation site, facilitates preferential nucleation of primary Mg_2Si near the sample edge and its subsequent growth toward the melt interior. Meanwhile, the alternating current in the induction coil induces currents in the electrically conductive Al-Mg-Si melt, and their interaction with the magnetic field generates Lorentz force-driven convection.

This forced flow continuously renews the solute boundary layer at the Mg_2Si/melt interface by transporting Mg- and Si-bearing liquid toward the crystallization front, which can reduce the effective thickness of the diffusion layer, thereby enhancing interfacial solute exchange, sustaining primary Mg_2Si growth, and influencing primary Mg_2Si dendrite coarsening behavior [66,67]. In addition, the conductivity contrast between the metallic melt and Mg_2Si can generate an electromagnetic expulsive(extrusion) force on suspended Mg_2Si particles that drives their migration relative to the melt. Therefore, primary Mg_2Si crystals that nucleate away from the sample edge are not retained as dispersed particles in the central melt, but are continuously transported, captured, and compacted toward the colder peripheral region. In the final stage, after primary Mg_2Si precipitation and electromagnetic-assisted peripheral enrichment, the Mg_2Si-rich layer becomes consolidated at the sample edge, while the remaining central melt solidifies into a primary Mg_2Si-depleted low-Si Al—Mg alloy.

3.4. Process integration

Vacuum distillation enables selective Mg removal from Al—Mg alloys due to the substantially higher volatility of Mg than Al. At 1273 K, the saturated vapor pressures of pure Al and Mg are 2.94×10^{-5} and 2.79×10^{4} Pa, respectively, differing by approximately nine orders of magnitude [68]. This substantial difference provides a strong thermodynamic basis for selective Mg evaporation, while previous studies have experimentally demonstrated effective Mg removal with high Al recovery [68–70]. The proposed Mg-assisted continuous electromagnetic fractional crystallization coupled with vacuum distillation offers an integrated upcycling route for converting Al—Si casting scrap into a high-value Al product, as schematically illustrated in Fig. 14. In this process, Mg is first added to the Al—Si scrap melt to transform Si from a difficult-

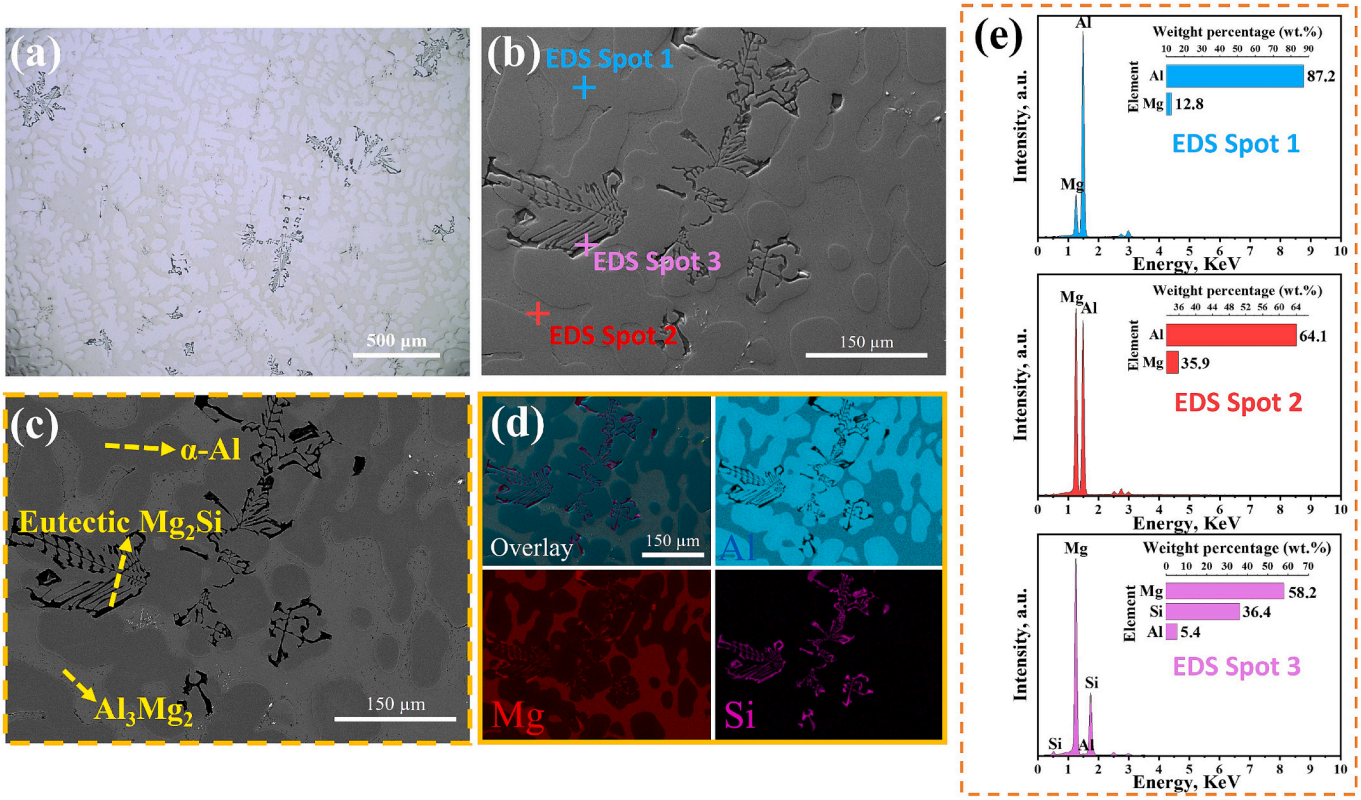


Fig. 12. Microstructural and compositional characterization of the primary Mg_2Si-depleted middle purified region of the #530 A sample: (a) optical micrograph; (b) SE-SEM image; (c) BSE-SEM image with EDS spot-analysis positions; (d) EDS elemental mappings of Al, Mg, and Si from the area shown in (c); and (e) EDS spectra and compositions of the selected phases.

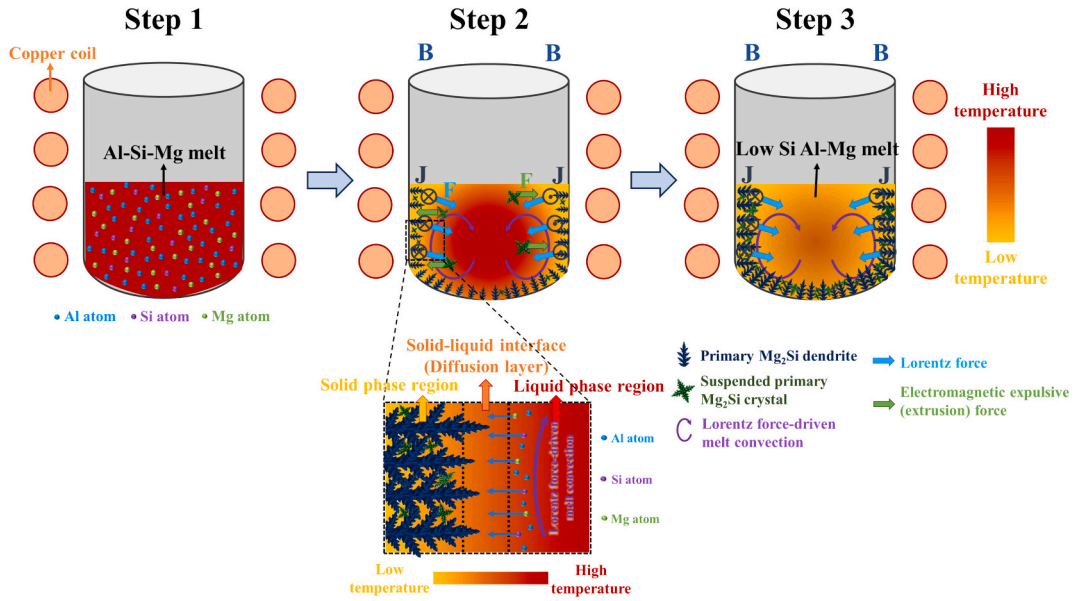


Fig. 13. Schematic illustration of the proposed mechanism of the Si removal through Mg-assisted continuous electromagnetic fractional crystallization.

to-separate eutectic constituent into separable primary Mg_2Si. Then, the primary Mg_2Si precipitated during the continuous electromagnetic fractional crystallization process promotes the outward migration and densification, thereby forming an Mg_2Si-rich peripheral layer, while the central region remains a low-Si Al—Mg melt. After crystallization, the Mg_2Si-rich solid fraction can be separated from the low-Si Al—Mg melt under hot-state solid-liquid separation conditions. The obtained low-Si Al—Mg melt is then subjected to vacuum distillation, where excess Mg is selectively evaporated and condensed for recovery, leaving an Al-rich residue as the target Al product. The recovered pure Mg can be used directly in other value-added applications or reintroduced into in the upstream crystallization process, where it again serves as a reactive medium for Si removal. This internal reuse reduces the requirement for fresh Mg addition and enhances the material circularity of the process.

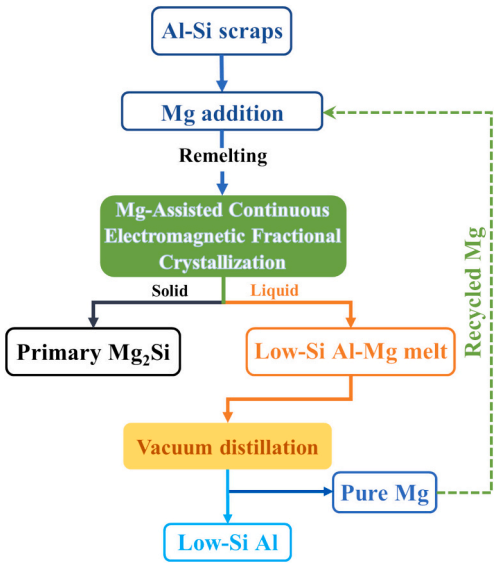


Fig. 14. Process flowchart for upcycling Al-Si alloy by Mg-assisted continuous electromagnetic fractional crystallization with vacuum.

Following residual-impurity control and composition adjustment, the Al-rich residue could serve as secondary feedstock for selected 5xxx and 6xxx-series wrought alloys used in electric vehicle bodies and battery pack structures.

4. Conclusion

This study developed an integrated upcycling strategy for Al—Si casting scrap through Mg-assisted continuous electromagnetic fractional crystallization, enabling selective Si removal and the recovery of high-value Al-rich products. Following Mg recovery and composition adjustment, the purified fraction could serve as secondary feedstock for selected low-Si 5xxx and 6xxx-series wrought alloys used in electric vehicle bodies and battery pack structures, thereby enabling the higher-value recycling of end-of-life automotive castings. The main conclusions are summarized as follows.

(1) Mg addition altered the phase precipitation sequence and promoted the transformation of Si from a difficult-to-separate eutectic constituent into separable primary Mg_2Si. At an Mg addition of 40% relative to the initial Al-9%Si alloy mass, thermochemical calculations predicted a theoretical Si removal efficiency of 93.7%.

(2) Continuous electromagnetic-field application during primary Mg_2Si precipitation promoted the migration, enrichment, and densification of primary Mg_2Si at the sample periphery, thereby substantially increasing the fraction of the central low-Si region without sacrificing its purification level. The purified-region area fraction increased from 71.2% at 330 A to 79.5% at 530 A, while the Si content remained around 0.4 wt%, corresponding to Si removal efficiencies of approximately 93.7%. The incremental improvement became more pronounced at higher current.

(3) The observed Si separation is attributed to the coupled effects of Mg-induced phase transformation, electromagnetic-field-driven melt convection, preferential Mg_2Si nucleation and growth near the colder crucible wall, and electromagnetic-force-assisted migration of primary Mg_2Si toward the peripheral region.

(4) The proposed Mg-assisted electromagnetic fractional crystallization enables efficient upcycling of Al-Si casting scrap, while recovery and reuse of Mg addition further support a low-waste circular recycling route.

Declaration of competing interest

The authors declare that they have no known competing financial interests or personal relationships that could have appeared to influence the work reported in this paper.

Acknowledgement

The authors gratefully acknowledge the China Scholarship Council (CSC, Grant No. 202306890034) for providing financial support to PhD candidate Mr. Bo Yang.

Appendix A. Supplementary data

Supplementary data to this article can be found online at https://doi.org/10.1016/j.seppur.2026.140736.

Data availability

Data will be made available on request.

References

[1] S.S. Li, X. Yue, Q.Y. Li, H.L. Peng, B.X. Dong, T.S. Liu, H.Y. Yang, J. Fan, S.L. Shu, F. Qiu, Q.C. Jiang, Development and applications of aluminum alloys for aerospace industry, J. Mater. Sci. Technol. 27 (2023) 944–983, https://doi.org/10.1016/j.jmrt.2023.09.274.

[2] E. Georgantzia, M. Gkantou, G.S. Kamaris, Aluminium alloys as structural material: a review of research, Eng. Struct. 227 (2021) 111372, https://doi.org/10.1016/j.engstruct.2020.111372.

[3] Z. Zhao, D. Li, X. Yan, Y. Chen, Z. Jia, D. Zhang, M. Han, X. Wang, G. Liu, X. Liu, S. Liu, Insights into the dual effects of Ti on the grain refinement and mechanical properties of hypoeutectic Al–Si alloys, J. Mater. Sci. Technol. 189 (2024) 44–59, https://doi.org/10.1016/j.jmst.2023.12.014.

[4] K.R. Ravi, R.M. Pillai, K.R. Amaranathan, B.C. Pai, M. Chakraborty, Fluidity of aluminum alloys and composites: a review, J. Alloys Compd. 456 (2008) 201–210, https://doi.org/10.1016/j.jallcom.2007.02.038.

[5] G. Niu, Y. Wang, L. Zhu, J. Ye, J. Mao, Fluidity of casting Al–Si series alloys for automotive light-weighting: a systematic review, Mater. Sci. Technol. 38 (2022) 902–911, https://doi.org/10.1080/02670836.2022.2068274.

[6] F. Lasagni, B. Mingler, M. Dumont, H.P. Degischer, Precipitation kinetics of Si in aluminium alloys, Mater. Sci. Eng. A 480 (2008) 383–391, https://doi.org/10.1016/j.msea.2007.07.008.

[7] S. Shankar, Y.W. Riddle, M.M. Makhlouf, Nucleation mechanism of the eutectic phases in aluminum–silicon hypoeutectic alloys, Acta Mater. 52 (2004) 4447–4460, https://doi.org/10.1016/j.actamat.2004.05.045.

[8] S. Hegde, K.N. Prabhu, Modification of eutectic silicon in Al–Si alloys, J. Mater. Sci. 43 (2008) 3009–3027, https://doi.org/10.1007/s10853-008-2505-5.

[9] A.K. Dahle, K. Nogita, S.D. McDonald, C. Dinnis, L. Lu, Eutectic modification and microstructure development in Al–Si alloys, Mater. Sci. Eng. A 413-414 (2005) 243–248, https://doi.org/10.1016/j.msea.2005.09.055.

[10] Y. Murakami, R. Furushima, K. Shiga, T. Miyajima, N. Omura, Mechanical property prediction of aluminium alloys with varied silicon content using deep learning, Acta Mater. 286 (2025) 120683, https://doi.org/10.1016/j.actamat.2024.120683.

[11] D. Raabe, D. Ponge, P.J. Uggowitzer, M. Roscher, M. Paolantonio, C. Liu, H. Antrekowitsch, E. Kozeschnik, D. Seidmann, B. Gault, F. De Geuser, A. Deschamps, C. Hutchinson, C. Liu, Z. Li, P. Prangnell, J. Robson, P. Shanthraj, S. Vakili, C. Sinclair, L. Bourgeois, S. Pogatscher, Making sustainable aluminum by recycling scrap: the science of "dirty" alloys, Prog. Mater. Sci. 128 (2022) 100947, https://doi.org/10.1016/j.pmatsci.2022.100947.

[12] International Aluminium Institute (IAI), Aluminium recycling saves 95% of the energy needed for primary aluminium production. https://international-aluminium.org/landing/aluminium-recycling-saves-95-of-the-energy-needed-for-primary-aluminium-production/ accessed March 15th 2026, 2026.

[13] S. Al-Alimi, N.K. Yusuf, A.M. Ghaleb, M.A. Lajis, S. Shamsudin, W. Zhou, Y. M. Altharan, H.S. Abdulwahab, Y. Saif, D.H. Didane, I.S.T.T.A. Adam, Recycling aluminium for sustainable development: a review of different processing technologies in green manufacturing, Results Eng. 23 (2024) 102566, https://doi.org/10.1016/j.rineng.2024.102566.

[14] K. Nakajima, O. Takeda, T. Miki, K. Matsubae, S. Nakamura, T. Nagasaka, Thermodynamic analysis of contamination by alloying elements in aluminum recycling, Environ. Sci. Technol. 44 (2010) 5594–5600, https://doi.org/10.1021/es9038769.

[15] A.N. Løvik, R. Modaresi, D.B. Müller, Long-term strategies for increased recycling of automotive aluminum and its alloying elements, Environ. Sci. Technol. 48 (2014) 4257–4265, https://doi.org/10.1021/es405604g.

[16] D. Raabe, C.C. Tasan, E.A. Olivetti, Strategies for improving the sustainability of structural metals, Nature 575 (2019) 64–74, https://doi.org/10.1038/s41586-019-1702-5.

[17] European Aluminium, Feasibility of aluminium component dismantling from ELV. 2021. https://european-aluminium.eu/wp-content/uploads/2022/08/irt-m2p-executive-sum-20210412-final-2.pdf. (accessed March 20th 2026).
[18] D. He, D.R. Keith, H.C. Kim, R. De Kleine, J. Anderson, M. Doolan, Materials challenges in the electric vehicle transition, Environ. Sci. Technol. 58 (2024) 12297–12303, https://doi.org/10.1021/acs.est.3c09042.
[19] E. Aluminium, Environmental Profile Report Life-Cycle Inventory Data for Aluminium Production and Transformation Processes in Europe, 2018.
[20] B. Wang, Z. Zhang, G. Xu, X. Zeng, W. Hu, K. Matsubae, Wrought and cast aluminum flows in China in the context of electric vehicle diffusion and automotive lightweighting, Resour. Conserv. Recycl. 191 (2023) 106877, https://doi.org/10.1016/j.resconrec.2023.106877.
[21] A. Rolseth, M. Carlson, E. Ghassemali, L. Pérez Caro, A.E.W. Jarfors, Impact of functional integration and electrification on aluminium scrap in the automotive sector: a review, Resour. Conserv. Recycl. 205 (2024) 107532, https://doi.org/10.1016/j.resconrec.2024.107532.
[22] S. Van den Eynde, E. Bracquené, D. Diaz-Romero, I. Zaplana, B. Engelen, J. R. Duflou, J.R. Peeters, Forecasting global aluminium flows to demonstrate the need for improved sorting and recycling methods, Waste Manag. 137 (2022) 231–240, https://doi.org/10.1016/j.wasman.2021.11.019.
[23] H. Hatayama, I. Daigo, Y. Matsuno, Y. Adachi, Evolution of aluminum recycling initiated by the introduction of next-generation vehicles and scrap sorting technology, Resour. Conserv. Recycl. 66 (2012) 8–14, https://doi.org/10.1016/j.resconrec.2012.06.006.
[24] M. Efe, A. Rohatgi, Q. Dai, B. Stapleton, K. Rader, A.L. Lipson, J.S. Spangenberger, Alloy selective optical sorting of mixed post-consumer aluminum scrap streams, Resour. Conserv. Recycl. 223 (2025) 108500, https://doi.org/10.1016/j.resconrec.2025.108500.
[25] D. Raabe, The materials science behind sustainable metals and alloys, Chem. Rev. 123 (2023) 2436–2608, https://doi.org/10.1021/acs.chemrev.2c00799.
[26] M.M. Makhlouf, H.V. Guthy, The aluminum–silicon eutectic reaction: mechanisms and crystallography, J. Light. Met. 1 (2001) 199–218, https://doi.org/10.1016/S1471-5317(02)00003-2.
[27] T. Tamura, M. Li, Separation of aluminum and silicon from crystallizing Al–12.6wt %Si eutectic melts by applying an electromagnetic force during directional solidification, J. Mater. Process. Technol. 342 (2025) 118916, https://doi.org/10.1016/j.jmatprotec.2025.118916.
[28] Y.K. Zhong, Y.L. Liu, K. Liu, L. Wang, L. Mei, J.K. Gibson, J.Z. Chen, S.L. Jiang, Y. C. Liu, L.Y. Yuan, Z.F. Chai, W.Q. Shi, In-situ anodic precipitation process for highly efficient separation of aluminum alloys, Nat. Commun. 12 (2021) 5777, https://doi.org/10.1038/s41467-021-26119-9.
[29] X. Lu, Z. Zhang, T. Hiraki, O. Takeda, H. Zhu, K. Matsubae, T. Nagasaka, A solid-state electrolysis process for upcycling aluminium scrap, Nature 606 (2022) 511–515, https://doi.org/10.1038/s41586-022-04748-4.
[30] B. Guo, Y. Wang, R. Li, Y. Li, B. Zhang, J. Peng, Y. Di, K. Wang, C. Wang, Sustainable recovery of pure aluminum from scrap aluminum alloy via soluble anode electrolysis: cathodic deposition behavior of Al and Mg ions in $MgCl_2$–KCl–NaCl molten salt system, J. Clean. Prod. 521 (2025) 146271, https://doi.org/10.1016/j.jclepro.2025.146271.
[31] B. Sun, N. Sun, L. Wang, S. Zhang, Z. Guo, A new process for efficient purification of 6061 aluminum alloy scrap under semi-solid and super-gravity conditions, J. Clean. Prod. 402 (2023) 136825, https://doi.org/10.1016/j.jclepro.2023.136825.
[32] B. Sun, L. Guo, Z. Wang, X. Lan, Z. Guo, Green extraction of pure aluminum from coarse AlSiCu alloys via centrifugal separation under isothermal semi-solid conditions: a novel upcycling strategy, Sep. Purif. Technol. 367 (2025) 132920, https://doi.org/10.1016/j.seppur.2025.132920.
[33] T. Tamura, M. Li, Upgrading recycling of Al–7 wt%Si alloys using electromagnetic force in directional solidification, J. Alloys Compd. 979 (2024) 173528, https://doi.org/10.1016/j.jallcom.2024.173528.
[34] M. Wang, S. Zhang, S. Du, J. Wang, B. Liu, A review of the upcycling of aluminum scrap and dross using molten salt electrolysis, Resour. Conserv. Recycl. 220 (2025) 108352, https://doi.org/10.1016/j.resconrec.2025.108352.
[35] Y. Zhang, Y. Lei, Y. Ren, W. Ma, Removal of Fe impurities from Al alloy scraps by electromagnetic directional solidification combined with Si addition, J. Mater. Sci. Technol. 26 (2023) 8738–8747, https://doi.org/10.1016/j.jmrt.2023.09.163.
[36] B. Yang, S. Friedrich, B. Friedrich, A novel upcycling strategy to Al alloys: Si removal via Mg-assisted suspension based fractional crystallization, Sep. Purif. Technol. 394 (2026) 137458, https://doi.org/10.1016/j.seppur.2026.137458.
[37] P.K. Galenko, D.V. Alexandrov, L.V. Toropova, Dendrite growth under a forced convective flow: a review, Phys. Rep. 1085 (2024) 1–48, https://doi.org/10.1016/j.physrep.2024.06.005.
[38] B. Yang, S. Friedrich, B. Friedrich, Advances in non-metallic inclusion removal from aluminum melts towards cleaner and higher-performance materials, J. Mater. Sci. 60 (2025) 12291–12314, https://doi.org/10.1007/s10853-025-11195-9.
[39] Z. Zhao, Y. Chai, S. Zheng, L. Wang, Y. Xiao, Electromagnetic field assisted metallic materials processing: a review, Steel Res. Int. 88 (2017) 1600273, https://doi.org/10.1002/srin.201600273.
[40] X. Li, A. Gagnoud, Z. Ren, Y. Fautrelle, R. Moreau, Investigation of thermoelectric magnetic convection and its effect on solidification structure during directional solidification under a low axial magnetic field, Acta Mater. 57 (2009) 2180–2197, https://doi.org/10.1016/j.actamat.2009.01.016.
[41] H. Zhang, M. Wu, C.M.G. Rodrigues, A. Ludwig, A. Kharicha, A. Rónaföldi, A. Roósz, Z. Veres, M. Svéda, Dendrite fragmentation mechanism under forced convection condition by rotating magnetic field during unidirectional solidification of AlSi7 alloy, Acta Mater. 241 (2022) 118391, https://doi.org/10.1016/j.actamat.2022.118391.
[42] X. Fan, N. Shevchenko, C. Tonry, S.J. Clark, R.C. Atwood, S. Eckert, K. Pericleous, P.D. Lee, A. Kao, Controlling solute channel formation using magnetic fields, Acta Mater. 256 (2023) 119107, https://doi.org/10.1016/j.actamat.2023.119107.
[43] Y. Sun, C. Li, Y. Liu, R. Ding, X. Liu, S.H. Kim, L. Yu, The contribution of aluminides to strength of Al–Mg2Si–cu–Ni alloys at room and elevated temperatures, Mater. Sci. Eng. A 817 (2021) 141381, https://doi.org/10.1016/j.msea.2021.141381.
[44] Y. Jin, H. Fang, R. Chen, S. Sun, S. Wang, Y. Su, J. Guo, Graded distribution and refinement of Mg2Si in Al–Mg2Si alloy prepared by traveling magnetic field, J. Mater. Sci. Technol. 24 (2023) 2319–2331, https://doi.org/10.1016/j.jmrt.2023.03.152.
[45] S. Eckert, P.A. Nikrityuk, B. Willers, D. Räbiger, N. Shevchenko, H. Neumann-Heyme, V. Travnikov, S. Odenbach, A. Voigt, K. Eckert, Electromagnetic melt flow control during solidification of metallic alloys, European Physical J. Special Topics 220 (2013) 123–137, https://doi.org/10.1140/epjst/e2013-01802-7.
[46] J. Yu, D. Du, Z. Ren, Y. Fautrelle, R. Moreau, X. Li, Influence of an axial magnetic field on microstructures and alignment in directionally solidified Ni-based superalloy, ISIJ Int. 57 (2017) 337–342, https://doi.org/10.2355/isijinternational.ISIJINT-2016-352.
[47] C. Puncreobutr, A.B. Phillion, J.L. Fife, P.D. Lee, Coupling in situ synchrotron X-ray tomographic microscopy and numerical simulation to quantify the influence of intermetallic formation on permeability in aluminium–silicon–copper alloys, Acta Mater. 64 (2014) 316–325, https://doi.org/10.1016/j.actamat.2013.10.044.
[48] S. Steinbach, L. Ratke, Melt flow in a mushy zone – barrier effect of intermetallic phases, Int. J. Cast Met. Res. 22 (2009) 290–293, https://doi.org/10.1179/136404609X367920.
[49] C.J. Song, Z.M. Xu, J.G. Li, Study on electromagnetic force for preparation of in-situ Al/Mg2Si functionally graded materials by electromagnetic separation method, Metall. Mater. Trans. B Process Metall. Mater. Process. Sci. 37 (2006) 1007–1014, https://doi.org/10.1007/BF02735023.
[50] D. Shu, T.X. Li, B.D. Sun, Y.H. Zhou, J. Wang, Z.M. Xu, Numerical calculation of the electromagnetic expulsive force upon nonmetallic inclusions in an aluminum melt: part I. Spherical particles, Metall. Mater. Trans. B Process Metall. Mater. Process. Sci. 31 (2000) 1527–1533, https://doi.org/10.1007/s11663-000-0037-8.
[51] N.S. Tiedje, J.A. Taylor, M.A. Easton, A new multi-zone model for porosity distribution in Al–Si alloy castings, Acta Mater. 61 (2013) 3037–3049, https://doi.org/10.1016/j.actamat.2013.01.064.
[52] X.R. Zhu, R.A. Harding, J. Campbell, Calculation of the free surface shape in the electromagnetic processing of liquid metals, Appl. Math. Model. 21 (1997) 207–214, https://doi.org/10.1016/S0307-904X(97)00008-5.
[53] A. Bansal, P. Chapelle, Y. Delannoy, E. Waz, P. Le Brun, J.P. Bellot, Experimental and numerical analysis of the deformation of a liquid aluminum free surface covered by an oxide layer during induction melting, Metall. Mater. Trans. B Process Metall. Mater. Process. Sci. 46 (2015) 2096–2109, https://doi.org/10.1007/s11663-015-0398-7.
[54] C. Li, Y.Y. Wu, H. Li, X.F. Liu, Morphological evolution and growth mechanism of primary Mg2Si phase in Al–Mg_2Si alloys, Acta Mater. 59 (2011) 1058–1067, https://doi.org/10.1016/j.actamat.2010.10.036.
[55] Q.D. Qin, Y.G. Zhao, Nonfaceted growth of intermetallic Mg2Si in Al melt during rapid solidification, J. Alloys Compd. 462 (2008) L28–L31, https://doi.org/10.1016/j.jallcom.2007.08.037.
[56] R. Arcaleni, A. Mantelli, L. Girelli, L. Tonelli, A. Morri, A. Pola, L. Ceschini, Microstructural characterization of primary and recycled aluminum AlSi7Mg alloy processed by the semi-solid thixocasting method, Mater. Charact. 220 (2025) 114657, https://doi.org/10.1016/j.matchar.2024.114657.
[57] M.H. Abdelaziz, A.M. Samuel, H.W. Doty, F.H. Samuel, Effect of morphological changes of eutectic Si particles on the ambient and high temperature tensile properties of Zr containing Al–Si alloys, J. Mater. Sci. Technol. 9 (2020) 5962–5981, https://doi.org/10.1016/j.jmrt.2020.04.001.
[58] B.H. Lee, S.H. Kim, J.H. Park, H.W. Kim, J.C. Lee, Role of Mg in simultaneously improving the strength and ductility of Al–Mg alloys, Mater. Sci. Eng. A 657 (2016) 115–122, https://doi.org/10.1016/j.msea.2016.01.089.
[59] X. Wang, Y. Lin, Z. Liu, S. Liu, Improving mechanical properties of a cast Al–Mg alloy with high Mg content by rapid solidification, Mater. Sci. Eng. A 852 (2022) 143709, https://doi.org/10.1016/j.msea.2022.143709.
[60] X. Zhang, D. Wang, H. Nagaumi, R. Wang, Z. Wu, X. Li, H. Zhang, Highly efficient Fe separation induced by Fe-containing particle agglomeration in Al-7Si-0.3Mg alloy melt, J. Mater. Sci. Technol. 21 (2022) 604–616, https://doi.org/10.1016/j.jmrt.2022.09.034.
[61] X.F. Wu, K.Y. Wang, F.F. Wu, R.D. Zhao, M.H. Chen, J. Xiang, S.N. Ma, Y. Zhang, Simultaneous grain refinement and eutectic Mg2Si modification in hypoeutectic Al-11Mg2Si alloys by Sc addition, J. Alloys Compd. 791 (2019) 402–410, https://doi.org/10.1016/j.jallcom.2019.03.326.
[62] X. Zhu, H. Yang, X. Dong, S. Ji, The effects of varying Mg and Si levels on the microstructural inhomogeneity and eutectic Mg2Si morphology in die-cast Al–Mg–Si alloys, J. Mater. Sci. 54 (2019) 5773–5787, https://doi.org/10.1007/s10853-018-03198-6.
[63] P. Biswas, D. Mandal, M.K. Mondal, Compressive failure analysis of in-situ Al-Mg2Si composites: experiment and finite element modelling, Eng. Fract. Mech. 277 (2023) 108986, https://doi.org/10.1016/j.engfracmech.2022.108986.
[64] J. Li, Q. An, S. Wu, F. Li, S. Lü, W. Guo, Relationship of Mg2Si morphology with Mg2Si content and its effect on properties of in-situ Mg2Si/Al–cu composites, J. Alloys Compd. 808 (2019) 151771, https://doi.org/10.1016/j.jallcom.2019.151771.

[65] C.-J. Song, Z.-M. Xu, J.-G. Li, Fabrication of in situ Al/Mg2Si functionally graded materials by electromagnetic separation method, Compos. A: Appl. Sci. Manuf. 38 (2007) 427–433, https://doi.org/10.1016/j.compositesa.2006.03.002.
[66] B. Ban, T. Zhang, J. Li, X. Bai, X. Pan, J. Chen, S. Hadi Tabaian, Solidification refining of MG-Si by Al-Si alloy under rotating electromagnetic field with varying frequencies, Sep. Purif. Technol. 202 (2018) 266–274, https://doi.org/10.1016/j.seppur.2018.03.069.
[67] H. Zhang, M. Wu, C.M.G. Rodrigues, A. Ludwig, A. Kharicha, Directional solidification of AlSi7Fe1 alloy under forced flow conditions: effect of intermetallic phase precipitation and dendrite coarsening, Metall. Mater. Trans. A 52 (2021) 3007–3022, https://doi.org/10.1007/s11661-021-06295-5.
[68] F. Chen, B. He, J. Sun, J. Yi, C. Cui, P. Qing, A. Cao, L. Chen, An efficient purification process for Al: synergistic treatment of waste-casting aluminum alloy by chemical deposition and vacuum distillation, J. Sustainable Metall. 11 (2025) 1722–1732, https://doi.org/10.1007/s40831-025-01076-5.
[69] J. Yi, B. He, J. Sun, P. Qing, A. Cao, X. Zhang, L. Chen, J. Xu, Innovative vacuum distillation technology for preparing refined Al from Al–Mg alloy, Sci. Rep. 14 (2024) 29823, https://doi.org/10.1038/s41598-024-81018-5.
[70] J. Pang, L. Kong, B. Yang, Eco-friendly recovery of strategic metallic resources: a vacuum-based distillation process for isolating and purifying Mg-Al-in, Mg-in, and Al-in alloy systems, J. Alloys Compd. 1037 (2025) 182345, https://doi.org/10.1016/j.jallcom.2025.182345.